A Semi-Implicit Compressible Model for Atmospheric Flows with Seamless Access to Soundproof and Hydrostatic Dynamics

TOMMASO BENACCHIO

MOX—Modelling and Scientific Computing, Dipartimento di Matematica, Politecnico di Milano, Milan, Italy

RUPERT KLEIN

FB Mathematik and Informatik, Freie Universität Berlin, Berlin, Germany

(Manuscript received 15 March 2019, in final form 20 August 2019)

ABSTRACT

When written in conservation form for mass, momentum, and density-weighted potential temperature, and with Exner pressure in the momentum equation, the pseudoincompressible model and the hydrostatic model only differ from the full compressible equations by some additive terms. This structural proximity is transferred here to a numerical discretization providing seamless access to all three analytical models. The semi-implicit second-order scheme discretizes the rotating compressible equations by evolving full variables, and, optionally, with two auxiliary fields that facilitate the construction of an implicit pressure equation. Time steps are constrained by the advection speed only as a result. Borrowing ideas on forward-in-time differencing, the algorithm reframes the authors' previously proposed schemes into a sequence of implicit midpoint step, advection step, and implicit trapezoidal step. Compared with existing approaches, results on benchmarks of nonhydrostatic- and hydrostatic-scale dynamics are competitive. The tests include a new planetary-scale gravity wave test that highlights the scheme's ability to run with large time steps and to access multiple models. The advancement represents a sizeable step toward generalizing the authors' acoustics-balanced initialization strategy to also cover the hydrostatic case in the framework of an all-scale blended multimodel solver.

1. Introduction

a. Motivation: Blending of full and reduced dynamical flow models

Atmospheric dynamics features a variety of scale-dependent motions that have been analytically described by scale analysis and asymptotics (Pedlosky 1992; Klein 2010). Reduced dynamical models emerging from the full compressible flow equations through generally singular asymptotic limits capture the essence of the phenomena of interest and reveal which effects are important – and which effects less so – for their description. Relevant examples include the anelastic and pseudoincompressible models, the quasigeostrophic and semigeostrophic models, and the hydrostatic primitive model equations (Hoskins and Bretherton 1972; Lipps and Hemler 1982; Durran 1989; Pedlosky 1992; Bannon 1996; Cullen and Maroofi 2003; Klein 2010).

Cullen (2007) argues that compressible atmospheric flow solvers should accurately reproduce the effective dynamics encoded by such reduced dynamical models with no degradation of solution quality as the respective limit regime is approached. Related numerical methods are known as *asymptotic preserving* or *asymptotically adaptive* schemes in the numerics literature, see Klein et al. (2001) and the review by Jin (2012) for references. If a scheme is designed such that it not only solves the compressible equations close to some limit regimes with the required accuracy but that it can also solve the limiting model equations when the respective asymptotic parameter is set to zero, this opens avenues to interesting applications and investigations.

Implementations of different model equations often use different numerical methods to represent identical terms. For example, in a comparison of a compressible model and a pseudoincompressible model, the former might discretize advection with a semi-Lagrangian scheme,

Denotes content that is immediately available upon publication as open access.

Corresponding author: Tommaso Benacchio, tommaso.benacchio@polimi.it

DOI: 10.1175/MWR-D-19-0073.1

while the latter uses a higher-order upwind finite volume formulation. In this case, differences in model results cannot be uniquely attributed to the differences in the underlying equations but may as well be influenced by the use of different advection schemes (see Smolarkiewicz and Dörnbrack 2008; Benacchio et al. 2014, for further examples).

Using a numerical method for the compressible equations that defaults to soundproof dynamics for vanishing Mach number, Benacchio et al. (2014) suggested an application in the context of well-balanced data assimilation. They implement a *blended* scheme that can be tuned to solve any one of a continuous family of equations that interpolate between the compressible and pseudoincompressible models, and use this feature to filter unwanted acoustic noise from some given or assimilated initial data. To properly capture a compressible flow situation with unknown balanced initial pressure distribution, they operate the scheme for some initial time steps in its pseudoincompressible mode and then relax the model blending parameter toward its compressible mode over a few more steps. In this fashion, the pseudoincompressible steps serve to find a balanced pressure field compatible with the velocity and potential temperature initial data, and the subsequent compressible flow simulation is essentially acoustics free. We remark that the pseudoincompressible and hydrostatic models are limits of the compressible equations for vanishing Mach number and aspect ratio, respectively.

Continuing this line of development, we describe in this paper a semi-implicit scheme that allows us to access the compressible, pseudoincompressible, and hydrostatic models within one and the same finite volume framework.

b. Related numerical schemes in the literature

A significant challenge in the dynamical description and forecast of weather and climate lies in the inherently multiscale nature of atmospheric flows. Driven by stratification and rotation, physical processes arise around a large-scale state of horizontally geostrophic, vertically hydrostatic balance. The compressible Euler equations are deemed the most comprehensive model to describe the resolved fluid dynamics of the system before parameterizations of unresolved processes are added. On the one hand, these equations allow for buoyancy-driven internal gravity wave and pressure-driven sound wave adjustments. On the other hand, meteorologically relevant features such as cyclones and anticyclones in the midlatitudes involve motions much slower than the sound speed, thus forcing numerical stiffness into discretizations of the compressible model in the low Mach number regime. As a result, most if not all numerical schemes used in operational weather forecasting employ varying degrees of implicitness or multiple time stepping that enable stable runs with long time step sizes unconstrained by sound speed [see, e.g., the reviews Marras et al. (2016); Mengaldo et al. (2019) and references therein for a list]. Typically, semi-implicit approaches integrate advective transport explicitly, then build an elliptic problem for the pressure variable (or, in other models, for the divergence) by combining the equations of the discrete system. The solution of the problem yields updates that are then replaced into the other variables.

Examples of operational dynamical cores using semi-implicit time-integration strategies are the European Centre for Medium-Range Weather Forecasts (ECMWF) IFS (Temperton et al. 2001; Hortal 2002), that discretizes the hydrostatic primitive equations, and the Met Office's ENDGame (Wood et al. 2014; Benacchio and Wood 2016). In particular, ENDGame uses a double-loop structure in the implicit solver entailing four solves per time step in its operational incarnation, a strategy carried over in recent developments (Melvin et al. 2019), and allowing the dynamical core to run stably and second-order accurately without additional numerical damping (in the operational setup, a small amount of off-centering is employed). By contrast, many other semi-implicit or time-split explicit discretizations use off-centering, divergence damping (Bryan and Fritsch 2002), or otherwise artificial diffusion in order to quell numerical instabilities. In nonoperational research, Dumbser et al. (2019), among others, present buoyancy- and acoustic-implicit second-order finite volume discretizations on staggered grids.

To simplify the formulation of the semi-implicit method, the equation set is often cast in terms of perturbations around an ambient state or a hydrostatically balanced reference state (see, e.g., Restelli and Giraldo 2009; Smolarkiewicz et al. 2014, 2019). However, as noted by Weller and Shahrokhi (2014), whose model does not use perturbations, large deviations from the reference state may question the assumptions underpinning the resulting system. The use of background or ambient states adds a priori knowledge that a model working with full variables would not need. Wood et al. (2014) and Melvin et al. (2019) use the model state computed at the previous time step as evolving background profile, although some readjustments are implemented to circumvent background states with unstable stratification. Bubnová et al. (1995)'s model, drawn on Laprise (1992), is based on full variables, yet retains basic state pressure also in the nonlinear version. While instabilities were later fixed as reported in Bénard et al. (2010), it remains unclear how to mitigate the additional computational costs associated with global nonhydrostatic modules in hydrostatic modeling frameworks [see, e.g., the direct comparison in Fig. 13 of Kühnlein et al. (2019)]. The numerical scheme presented in this paper can operate both on a full-variable formulation and a perturbation-variable formulation of the implicit substep.

The FVM model (Kühnlein et al. 2019), an alternative next-generation ECMWF dynamical core, uses a finite volume discretization to address the potential efficiency issues caused by spectral transforms in IFS at increasing global resolutions. The time integration algorithm in FVM builds on extensive earlier experience with the EULAG model and the MPDATA advection scheme. Through appropriate correction of a first-order upwind discretization, a system is constructed that encompasses transport and implicit dynamics in an elegant analytical and numerical framework (Smolarkiewicz et al. 2014, 2016, and references therein). The approach, which in its default configuration relies on time extrapolation of advecting velocities and subtraction of reference states, also contains soundproof analytical systems as subcases and has shown excellent performance in integrating atmospheric flows at all scales without instabilities. However, their transition from compressible to soundproof discretizations is not seamless in the sense of the present work, since the structure of their implicit pressure equations substantially differs from one model to the other (but does take into account accurate treatment of boundary conditions and forces). Similarly to the present approach, an optional variant of their scheme avoids extrapolations in time from earlier time levels.

Drawing on the finite volume framework for soundproof model equations in Klein (2009), the authors of Benacchio (2014); Benacchio et al. (2014) devised a numerical scheme for the compressible Euler equations to simulate small- to mesoscale atmospheric motions, using a time step unconstrained by the speed of acoustic waves within the abovementioned soundproof-compatible switchable multimodel formulation. The underlying theoretical framework was extended by Klein and Benacchio (2016) to incorporate the hydrostatic primitive equations and the anelastic, quasi-hydrostatic system of Arakawa and Konor (2009) with the introduction of a second blending parameter.

A major hurdle toward applying the numerical scheme of Benacchio et al. (2014) to the theoretical setup of Klein and Benacchio (2016) is the former's time step dependency on the speed of internal gravity waves, a severe constraint on the applicability of the numerical method to large-scale tests. The present study addresses this fundamental shortcoming.

c. *Contribution*

By reframing the schemes of Klein (2009) and Benacchio et al. (2014) as a two-stage-implicit plus transport system, this paper proposes an original set of features within a discretization that:

- Evolves the compressible equations with rotation in terms of full variables, using auxiliary potential temperature and Exner pressure variables in casting the buoyancy-implicit substep;
- Provides discretely equivalent full-variable and perturbation-variable formulations of the implicit substep;
- Operates with conservative advection of mass, momentum, and mass-weighted potential temperature, and is second-order accurate in all components, without the need for additional diffusion;
- Uses a time step constrained only by the underlying advection speed;
- Works with a node-based implicit pressure equation only, thus avoiding a cell-centered MAC-projection (see Almgren et al. 1998; Benacchio et al. 2014, and references therein);
- Can be operated in the soundproof and hydrostatic modes without modifying the numerics;
- Constitutes a basis for a multiscale formulation with access to hydrostasy and geostrophy.

The method uses explicit second-order MUSCL scheme for advection (Van Leer 2006), while the pressure and momentum equations are stably integrated by solving two elliptic problems embedded in the implicit midpoint and implicit trapezoidal stages. A hydrostatic switch, also available within the ENDGame model (Melvin et al. 2010), is added to the soundproof switch of Benacchio et al. (2014), enabling evaluation of three analytical systems of equations under the same numerical framework.

The scheme is validated against two-dimensional Cartesian benchmarks of nonhydrostatic and hydrostatic dynamics. Simulations of gravity wave tests at large scale and with rotation show good solution quality relative to existing approaches already at relatively coarse resolutions. In particular, a new planetary-scale extension of the hydrostatic-scale test of Skamarock and Klemp (1994) showcases the large time step capabilities of the present scheme.

Exploiting the multimodel character of the numerical framework, the model is also run in pseudoincompressible mode and hydrostatic mode and analyze the difference with the compressible simulation. As expected from theoretical normal mode analyses [Davies et al. (2003); Dukowicz (2013), though see also Klein et al. (2010) for a discussion on regime of validity of soundproof models], the compressible/hydrostatic discrepancy shrinks with smaller vertical-to-horizontal domain size aspect ratios, while the compressible/pseudoimcompressible discrepancy grows. Note also that Smolarkiewicz et al. (2014) demonstrated much larger discrepancies between compressible and anelastic results than between compressible and pseudoincompressible results for a large-scale baroclinic wave test. They traced the effect back to the linearization of the pressure gradient term that occurs in the anelastic model but not in the pseudoincompressible model.

The paper is organized as follows. Section 2 contains the governing equations that are discretized with the methodology summarized in section 3 and detailed in section 4. Section 5 documents the performance of the code on the abovementioned tests. Results are discussed and conclusions drawn in section 6.

2. Governing equations

The governing equations for adiabatic compressible flow of an inert ideal gas with constant specific heat capacities under the influence of gravity and in a rotating coordinate system corresponding to a tangent plane approximation may be written as

$$\rho_t + \nabla_\parallel \cdot (\rho\mathbf{u}) + (\rho w)_z = 0, \tag{1a}$$

$$(\rho\mathbf{u})_t + \nabla_\parallel \cdot (\rho\mathbf{u}\circ\mathbf{u}) + (\rho w\mathbf{u})_z = -[c_p P\nabla_\parallel \pi + f(y)\mathbf{k}\times\rho\mathbf{u}], \tag{1b}$$

$$(\rho w)_t + \nabla_\parallel \cdot (\rho\mathbf{u}w) + (\rho w^2)_z = -(c_p P\pi_z + \rho g), \tag{1c}$$

$$P_t + \nabla_\parallel \cdot (P\mathbf{u}) + (Pw)_z = 0. \tag{1d}$$

Here ρ is the density, $\mathbf{u} = (u, v)$ and w are the horizontal and vertical components of the velocity,

$$\pi = \left(\frac{p}{p_{\mathrm{ref}}}\right)^{R/c_p} \quad \text{and} \quad P = \frac{p_{\mathrm{ref}}}{R}\left(\frac{p}{p_{\mathrm{ref}}}\right)^{c_v/c_p} \equiv \rho\Theta \tag{2}$$

are the Exner pressure and the mass-weighted potential temperature, with p_{ref} a suitable reference pressure, R the gas constant, and c_p and $c_v = c_p - R$ the specific heat capacities at constant pressure and constant volume. Furthermore, g is the acceleration of gravity (taken as constant), $f(y) = f_0 + \beta y$ the local Coriolis parameter in the β plane with constant f_0 and β, $\mathbf{k}$ the vertical unit vector, and $\times$ the cross product. Subscripts as in $U_x \equiv \partial_x U := \partial U/\partial x$ denote partial derivatives with respect to the first coordinate of a Cartesian (x, y, z) coordinate system or time t, and $\nabla_\parallel = (\partial_x, \partial_y, 0)$ subsumes the horizontal derivatives.

Given (1a) and (1d), the potential temperature $\Theta = P/\rho$ satisfies the usual advection equation:

$$\Theta_t + \mathbf{u}\cdot\nabla_\parallel\Theta + w\Theta_z = 0. \tag{3}$$

3. Compact description of the time integration scheme

In this section we describe the main structural features of the discretization, which evolves and joins aspects of the models in Klein (2009); Benacchio et al. (2014), and borrows key ideas from the forward-in-time integration strategy suggested by Smolarkiewicz and Margolin (1993, 1997) in realizing the implicit discretization of the gravity term.

a. *Reformulation of the governing equations*

1) Evolution of the primary variables

The primary unknowns advanced in time by the present scheme are the same as in (1) [i.e., $(\rho, \rho\mathbf{u}, \rho w, P)$]. Introducing a seamless blended discretization of the compressible Euler and pseudoincompressible equations (Durran 1989) and following Klein (2009); Klein et al. (2010), in Benacchio et al. (2014) the authors observed that the pseudoincompressible model is obtained from the compressible equations in (1) by simply dropping the time derivative of $P = \rho\Theta$ from (1d). To take advantage of this close structural model relationship in constructing a blended scheme that can be tuned seamlessly from solving the full compressible to solving the pseudoincompressible model equations, they introduced the inverse of the potential temperature,

$$\chi = 1/\Theta, \tag{4}$$

and interpreted the mass balance (1a) as a transport equation for χ:

$$\rho_t + \nabla_\parallel \cdot (\rho\mathbf{u}) + (\rho w)_z = (P\chi)_t + \nabla_\parallel \cdot (P\chi\mathbf{u}) + (P\chi w)_z = 0. \tag{5}$$

Here the field $(P\mathbf{v})$, $\mathbf{v} = (\mathbf{u}, w)$, takes the role of an advecting flux. Using this interpretation throughout the equations and introducing two blending parameters, α_w and α_P, for the nonhydrostatic/hydrostatic and compressible/pseudoincompressible transitions, one obtains

$$\rho_t + \nabla_\parallel \cdot (P\mathbf{u}\chi) + (Pw\chi)_z = 0, \tag{6a}$$

$$(\rho\mathbf{u})_t + \nabla_\parallel \cdot (P\mathbf{u} \circ \chi\mathbf{u}) + (Pw\chi\mathbf{u})_z = -[c_p P \nabla_\parallel \pi + f(y)\mathbf{k} \times \rho\mathbf{u}], \tag{6b}$$

$$\alpha_w[(\rho w)_t + \nabla_\parallel \cdot (P\mathbf{u}\chi w) + (Pw\chi w)_z] = -(c_p P \pi_z + \rho g), \tag{6c}$$

$$\alpha_P P_t + \nabla_\parallel \cdot (P\mathbf{u}) + (Pw)_z = 0. \tag{6d}$$

System (6) is the analytical formulation used in this paper, and it facilitates the extension of the blending of Benacchio et al. (2014) to hydrostasy along the lines of the theory described in Klein and Benacchio (2016). The quasigeostrophic case will be addressed in forthcoming work.

2) Auxiliary perturbation variables and their evolution equations

A crucial ingredient of any numerical scheme implicit with respect to the effects of compressibility, buoyancy, and Earth rotation, is that it has separate access to the large-scale mean background stratification of potential temperature, or its inverse. Many schemes found in the literature use perturbation variables to realize such access, and the reference implementation of our scheme described in this section is also constructed this way. Yet, we demonstrate in appendix D that the scheme can be formulated equivalently working with full variables only.

For the formulation with perturbation variables, the Exner pressure π and inverse potential temperature χ are split into

$$\pi(t,\mathbf{x},z) = \pi'(t,\mathbf{x},z) + \overline{\pi}(z) \quad \text{and} \quad \chi(t,\mathbf{x},z) = \chi'(t,\mathbf{x},z) + \overline{\chi}(z), \tag{7}$$

with the hydrostatically balanced background variables satisfying

$$\frac{d\overline{\pi}}{dz} = -\frac{g}{c_p}\overline{\chi} \quad \text{and} \quad \overline{\pi}(0) = 1. \tag{8}$$

Since, for the compressible case, P can be expressed as a function of π alone according to expression (2), and since $\overline{\pi}$ is time independent across a time step, the perturbation Exner pressure satisfies

$$\alpha_P\left(\frac{\partial P}{\partial \pi}\right)\pi'_t = -\nabla \cdot [P(\pi)\mathbf{v}], \tag{9}$$

which is a direct consequence of (6d). In turn, the perturbation form of the mass balance serves as the evolution equation for χ', from (5) and (7)

$$(P\chi')_t + \nabla_\parallel \cdot (P\mathbf{u}\chi') + (Pw\chi')_z = -Pw\overline{\chi}_z. \tag{10}$$

Auxiliary discretizations of (9) and (10) will be used in constructing a numerical scheme for the full variable form of the governing equations in (6) that is stable for time steps limited only by the advection Courant number. In the current implementation of the scheme, the perturbation Exner pressure variable is actually evolved in time redundantly to the pressure-like variable P as this yielded the most robust and accurate results. A similar redundancy of an Exner pressure variable was also found advantageous in ECMWF's FVM module (see Kühnlein et al. 2019, and references therein).

In the sequel, borrowing notation from Smolarkiewicz et al. (2014), we introduce

$$\Psi = (\chi, \chi\mathbf{u}, \chi w, \chi') \tag{11}$$

and subsume the primary equations in (6) and the auxiliary equation for χ' in (10) as

$$(P\Psi)_t + \mathscr{A}(\Psi; P\mathbf{v}) = Q(\Psi; P) \tag{12a}$$

$$\alpha_P P_t + \nabla \cdot (P\mathbf{v}) = 0. \tag{12b}$$

Note that the π' equation in (9) is equivalent to (12b) and thus it is not listed separately, although it will be used in an auxiliary step in the design of a stable discretization of (12b).

b. *Semi-implicit time discretization*

1) Implicit midpoint pressure update and advective fluxes

In the first step of the scheme, we determine advective fluxes at the half-time level, $(P\mathbf{v})^{n+1/2}$, which for $\alpha_P = 1$ immediately yield the update of the internal energy variable, P, through

$$\alpha_P(P^{n+1} - P^n) = -\Delta t \tilde{\nabla} \cdot (P\mathbf{v})^{n+1/2}, \tag{13}$$

where $\tilde{\nabla}$ is the discrete approximation of the divergence. In contrast, for $\alpha_P = 0$ this equation represents the pseudoincrompressible divergence constraint.

Note that in the compressible case this update corresponds to a time discretization of the P equation using the *implicit midpoint rule*. We recall here for future reference that an implementation of the implicit midpoint rule can be achieved by first applying a half time step based on the implicit Euler scheme followed by another half time step based on the explicit Euler method (Hairer et al. 2006). First-order accurate time integration is sufficient for generating the half-time level fluxes, see appendix A for details.

To achieve stability for large time steps, only limited by the advection Courant number, we invoke standard splitting into advective and nonadvective terms in (6), (10) for the prediction of $(P\mathbf{v})^{n+1/2}$, with explicit advection and linearly implicit treatment of the right-hand sides. Thus we first advance the scalars from (11) by half an advection time step using advective fluxes computed at the old time level:

$$(P\Psi)^{\#} = \mathscr{A}_{1\text{st}}^{\Delta t/2}[\Psi^n; (P\mathbf{v})^n] \tag{14a}$$

$$P^{\#} = P^n - \frac{\Delta t}{2}\widetilde{\nabla}\cdot(P\mathbf{v})^n. \tag{14b}$$

Here $\mathscr{A}_{1\text{st}}^{\Delta t}$ denotes an at least first-order accurate version of our advection scheme for the Ψ variables given the advecting fluxes $(P\mathbf{v})^n$, see section 4b for details. In the pseudoincompressible case the discretization guarantees that $(P\mathbf{v})^n$ is discretely divergence free as shown below, so that $P^{\#} = P^n$ and the α_P parameter need not be explicitly noted in (14b).

Next, the half-time level fluxes $(P\mathbf{v})^{n+1/2}$ are obtained via the implicit Euler discretization of a second split system that only involves the right-hand sides of (6) (see section 4c below for details):

$$(P\Psi)^{n+1/2} = (P\Psi)^{\#} + \frac{\Delta t}{2}Q(\Psi^{n+1/2}; P^{n+1/2}), \tag{15a}$$

$$\alpha_P P^{n+1/2} = \alpha_P P^n - \frac{\Delta t}{2}\nabla\cdot(P\mathbf{v})^{n+1/2}. \tag{15b}$$

We note that for $\alpha_P = 1$ (15b) corresponds to the implicit Euler update of P to the half-time level (i.e., to the first step of our implementation of the implicit midpoint rule for this variable). Furthermore, as in Benacchio et al. (2014), in this step the relation between P, which is being updated by the flux divergence, and π, whose gradient is part of the momentum forcing terms, is approximated through a linearization of the equation of state (2):

$$P^{n+1/2} = P^n + \left(\frac{\partial P}{\partial \pi}\right)^{\#}(\pi^{n+1/2} - \pi^n). \tag{16}$$

With this linearization, this implicit Euler step involves a single linear elliptic solve for $\pi^{n+1/2}$. Optionally, an outer iteration of the linearly implicit step can be invoked to guarantee consistency with the equation of state for $P(\pi)$ up to a given tolerance.

These preliminary calculations serve to provide the fluxes $(P\mathbf{v})^{n+1/2}$ later needed both for the final explicit Euler update of P to the full time level t^{n+1} and for the advection of the vector of specific variables Ψ from (11) as part of the overall time stepping algorithm, see (17b) below.

For $\alpha_P = 0$ the P equation reduces to the pseudoincompressible divergence constraint, and P and the Exner pressure π decouple. While $P \equiv \overline{P}(z)$ remains constant in time in this case, increments of π correspond to the elliptic pressure field that guarantees compliance of the velocity with the divergence constraint.

2) Implicit trapezoidal rule along explicit Lagrangian paths for advected quantities

Given the advective fluxes, $(P\mathbf{v})^{n+1/2}$, the full second-order semi-implicit time step for the evolution equation of the advected scalars, Ψ, reads as follows:

$$(P\Psi)^{*} = (P\Psi)^n + \frac{\Delta t}{2}Q(\Psi^n; P^n), \tag{17a}$$

$$(P\Psi)^{**} = \mathscr{A}_{2\text{nd}}^{\Delta t}[\Psi^{*}; (P\mathbf{v})^{n+1/2}], \tag{17b}$$

$$(P\Psi)^{n+1} = (P\Psi)^{**} + \frac{\Delta t}{2}Q(\Psi^{n+1}; P^{n+1}), \tag{17c}$$

$$\alpha_P P^{n+1} = \alpha_P P^n - \Delta t\nabla\cdot(P\mathbf{v})^{n+1/2}. \tag{17d}$$

Here we notice that the homogeneous Eqs. (1a) and (1d) for ρ and P are not involved in (17a) and (17c). The updates to ρ^{n+1} and P^{n+1} are entirely determined by the advection step in (17b) and by the completion of the implicit midpoint discretization of the P equation in (17d).

Therefore, the updated unknowns in the explicit and implicit Euler steps (17a) and (17c) are $(\mathbf{u}, w, \chi')$ only. Nevertheless, in order to obtain an appropriate approximation of the Exner pressure gradient needed in the momentum equation, an auxiliary implicit Euler discretization of the energy equation in perturbation form for π' from (9) is used in formulating (17c). See section 4c for details.

After completion of the steps in (17) we have two redundancies in the thermodynamic variables. In addition to the primary variables (ρ, P), we also have the perturbation inverse potential temperature, χ', and the Exner pressure increment π'. The redundancy in χ' is trivially removed by resetting the variable after each time step to $\chi' = \rho/P - \overline{\chi}$, while the redundancy in the auxiliary Exner pressure is maintained throughout the time integration. See also section 4d.

Note that the implicit trapezoidal step (17) and to a lesser extent the treatment of P in (14), (15b), and (17d), closely resemble the EULAG/FVM forward-in-time discretization from Smolarkiewicz and Margolin (1997), Prusa et al. (2008), Smolarkiewicz et al. (2014, 2016), and Kühnlein et al. (2019).

We emphasize that (17a)–(17c) (i.e., the combination of an explicit Euler step for the fast modes, an advection step, and a final implicit Euler step for the fast modes), is *not* a variant of Strang's operator splitting strategy (Strang 1968). To achieve second-order accuracy, Strang splitting requires all substeps of the split algorithm to be second-order accurate individually, aside from being applied in the typical alternating sequence. This condition is not satisfied here as the initial explicit Euler step and final implicit Euler step are both only first-order accurate. As shown by Smolarkiewicz and Margolin (1993), second-order accuracy results here from a structurally different cancellation of truncation errors than in Strang's argument: by interleaving the Euler steps (17a) and (17c) with a full time step of second-order advection in (17b), one effectively applies the implicit trapezoidal (or Crank–Nicolson) discretization *along the Lagrangian trajectories* that are implicitly described by the finite-volume advection scheme, and this turns out to be second-order accurate if the trajectories (i.e., the advection step) are so.

4. Discretization details

a. Cartesian grid arrangement

The space discretization of the present scheme for the primary and auxiliary solution variables

$$\mathscr{U} = (\rho, \rho\mathbf{u}, \rho w, P, P\chi')^{\mathrm{T}} \tag{18}$$

is centered on control volumes $C_{i,j,k}$ formed by a Cartesian mesh with constant, but not necessarily equal, grid spacings $\Delta x, \Delta y, \Delta z$, and grid indices $i = 0, \ldots, I-1$, $j = 0, \ldots, J-1, k = 0, \ldots, K-1$ in the three coordinate directions (Fig. 1 shows a two-dimensional slice). The discrete numerical solution consists of approximate gridcell averages:

$$\mathscr{U}^n_{i,j,k} \approx \frac{1}{\Delta x \Delta y \Delta z}\int_{C_{i,j,k}} \mathscr{U}(\mathbf{x}, t^n)\, d^3\mathbf{x}. \tag{19}$$

The scheme is second-order accurate (see appendix B for empirical corroboration), so that we can interchangeably interpret $\mathscr{U}^n_{i,j,k}$ as the cell average or as a point value of $\mathscr{U}$ at the center of mass of a cell within the approximation order.

Advection of the specific variables Ψ defined in (11) is mediated by staggered-grid components of the advective flux field $(P\mathbf{v})^{n+1/2}$ referred to in section 3b above.

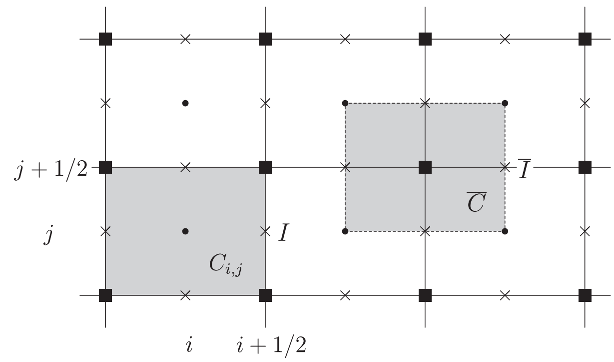

FIG. 1. Cartesian grid arrangement for two space dimensions. $C_{i,j}$: primary finite volumes, ●: primary cell centers, I: primary cell interfaces, ×: centers of both primary and dual cell interfaces, $\overline{C}$: dual cells for nodal pressure computation, ■: dual cell centers, and $\overline{I}$: dual cell interfaces.

Specifically, the fluxes $(Pu\Psi)^{n+1/2}_{i+1/2,j,k}$, $(Pv\Psi)^{n+1/2}_{i,j+1/2,k}$, and $(Pw\Psi)^{n+1/2}_{i,j,k+1/2}$ are defined on cell faces $I_{i+1/2,j,k}$, $I_{i,j+1/2,k}$, and $I_{i,j,k+1/2}$ (Fig. 1). Given, for example, $(Pu\Psi)^{n+1/2}_{i+1/2,j,k}$, the associated $\Psi^{n+1/2}_{i+1/2,j,k}$ is determined by a monotone upwind scheme for conservation laws [MUSCL, Van Leer (2006)] as described below. Finally, the perturbation Exner pressure used in (9) is stored at the nodes.

b. Advection

Any robust numerical scheme capable of performing advection of a scalar in compressible flows is a good candidate for the generic discrete advection operators $\mathscr{A}^{\Delta t}_{\mathrm{1st}}$ and $\mathscr{A}^{\Delta t}_{\mathrm{2nd}}$ introduced in (14a) and (17b). The present implementation is based on a directionally Strang-split monotone upwind scheme for conservation laws [MUSCL, see, e.g., Van Leer (2006)]:

Suppose the half-time predictor step from (15), the details of which are given in section 4c(3) below, has been completed. Then the components of the advecting fluxes $(P\mathbf{v})^{n+1/2}$ at gridcell faces have become available as part of this calculation. Given these fluxes, the advection step in (17b) is discretized via Strang splitting, so that

$$\begin{aligned}\mathscr{U}^{**}_{i,j} &= \mathscr{A}^{\Delta t}_{\mathrm{2nd}}\mathscr{U}^{*}_{i,j,k} \\ &\equiv \mathscr{A}^{\Delta t/2}_{x}\mathscr{A}^{\Delta t/2}_{y}\mathscr{A}^{\Delta t/2}_{z}\mathscr{A}^{\Delta t/2}_{z}\mathscr{A}^{\Delta t/2}_{y}\mathscr{A}^{\Delta t/2}_{x}\mathscr{U}^{*}_{i,j},\end{aligned} \tag{20}$$

where, dropping the indices of the transverse directions for simplicity, we have, for example,

$$\mathscr{A}^{\Delta t/2}_{x}\mathscr{U}_{i} = \mathscr{U}_{i} - \frac{\Delta t}{2\Delta x}[(Pu)^{n+1/2}_{i+1/2}\Psi_{i+1/2} - (Pu)^{n+1/2}_{i-1/2}\Psi_{i-1/2}], \tag{21}$$

with

$$\Psi_{i+1/2} = \sigma\Psi^-_{i+1/2} + (1-\sigma)\Psi^+_{i+1/2}, \tag{22a}$$

$$\sigma = \mathrm{sign}[(Pu)^{n+1/2}_{i+1/2}], \tag{22b}$$

$$\Psi^-_{i+1/2} = \Psi_i + \frac{\Delta x}{2}(1 - C^{n+1/2}_{i+1/2})s_i, \tag{22c}$$

$$\Psi^+_{i+1/2} = \Psi_{i+1} - \frac{\Delta x}{2}(1 + C^{n+1/2}_{i+1/2})s_{i+1}, \tag{22d}$$

$$C^{n+1/2}_{i+1/2} = \frac{\Delta t}{\Delta x}\frac{(Pu)^{n+1/2}_{i+1/2}}{(P_i + P_{i+1})/2}, \tag{22e}$$

$$s_i = \mathrm{Lim}\left(\frac{\Psi_i - \Psi_{i-1}}{\Delta x}, \frac{\Psi_{i+1} - \Psi_i}{\Delta x}\right), \tag{22f}$$

where P_i in (22e) denotes the fourth component of $\mathscr{U}_i$, and Lim(a, b) is a slope limiting function (see, e.g., Sweby 1984).

Importantly, the advecting fluxes $(P\mathbf{v})^{n+1/2}$ are maintained unchanged throughout the Strang splitting cycle for advection (20). In addition, it is not difficult to prove analytically that a constant advected scalar remains constant no matter whether we control the divergence of the advective fluxes very tightly or not at all, see appendix C for corroboration.

The first-order accurate advection operator $\mathscr{A}^{\Delta t}_{\mathrm{1st}}$ used in (14) is a simplified version of the above in that the advective fluxes are approximated at the old time level [i.e., the cell-to-face interpolation formulae for the advective fluxes described in section 3 below are evaluated with the components of $(P\mathbf{v})^n$]. Optionally, one may also use simple $\mathscr{A}^{\Delta t}_z \mathscr{A}^{\Delta t}_y \mathscr{A}^{\Delta t}_x$-splitting instead of the full Strang cycle from (20) for the advection step of this predictor. In the test shown below we have used the full Strang cycle throughout.

c. *Semi-implicit integration of the forcing terms*

The generalized forcing terms on the right-hand side of (6) are discretized in time by the implicit trapezoidal rule. This requires an explicit Euler step at the beginning and an implicit Euler step at the end of a time step. The implicit Euler scheme is also used to compute the fluxes $(P\mathbf{v})^{n+1/2}$ at the half-time level as needed for the advection substep. Below we summarize this implicit step in a temporal semidiscretization, explain how this step is used to access the hydrostatic and pseudoincompressible balanced models seamlessly and provide the node-based spatial discretization, and explain how the divergence-controlled momenta are used to generate divergence controlled advective fluxes across the faces of the primary control volumes.

1) Implicit Euler step and access to hydrostatic and soundproof dynamics

Both ρ and P are frozen in time in this split step because their evolution Eqs. (6a) and (6d) do not carry a right-hand side. Hence, the linearized equations including the auxiliary potential temperature perturbation equation (10) as well as the hydrostatic and pseudoincompressible switches, α_w and α_P may be written as

$$U_t = -c_p(P\Theta)^\circ \pi'_x + fV, \tag{23a}$$

$$V_t = -c_p(P\Theta)^\circ \pi'_y - fU, \tag{23b}$$

$$\alpha_w W_t = -c_p(P\Theta)^\circ \pi'_z - g\frac{\tilde{\chi}}{\chi^\circ}, \tag{23c}$$

$$\tilde{\chi}_t = -W\frac{d\overline{\chi}}{dz}, \tag{23d}$$

$$\alpha_P\left(\frac{\partial P}{\partial \pi}\right)^\circ \pi'_t = -U_x - V_y - W_z, \tag{23e}$$

where $(U, V, W, \tilde{\chi}) = (Pu, Pv, Pw, P\chi')$ and where $(P\Theta)^\circ$, χ°, and $(\partial P/\partial \pi)^\circ$ are either those values available when the routine solving the implicit Euler step is called or those adjusted nonlinearly in an outer iteration loop as described in a similar context by Smolarkiewicz et al. (2014). In this paper we have used the simpler variant without an outer iteration throughout.

The implicit Euler semidiscretization of (23) in time then reads as follows:

$$U^{n+1} = U^n - \Delta t[c_p(P\Theta)^\circ \pi'^{n+1}_x - fV^{n+1}], \tag{24a}$$

$$V^{n+1} = V^n - \Delta t[c_p(P\Theta)^\circ \pi'^{n+1}_y + fU^{n+1}], \tag{24b}$$

$$\alpha_w W^{n+1} = \alpha_w W^n - \Delta t\left[c_p(P\Theta)^\circ \pi'^{n+1}_z + g\frac{\tilde{\chi}^{n+1}}{\chi^\circ}\right], \tag{24c}$$

$$\tilde{\chi}^{n+1} = \tilde{\chi}^n - \Delta t\frac{d\overline{\chi}}{dz}W^{n+1}, \tag{24d}$$

$$\alpha_P\left(\frac{\partial P}{\partial \pi}\right)^\circ \pi'^{n+1} = \alpha_P\left(\frac{\partial P}{\partial \pi}\right)^\circ \pi'^n - \Delta t(U^{n+1}_x + V^{n+1}_y + W^{n+1}_z). \tag{24e}$$

Straightforward manipulations yield the new time level velocity components:

$$\begin{pmatrix} U \\ V \end{pmatrix}^{n+1} = \frac{1}{1+(\Delta t f)^2}\left[\begin{pmatrix} U + \Delta t f V \\ V - \Delta t f U \end{pmatrix}^n - \Delta t c_p (P\Theta)^\circ \begin{pmatrix} \pi'_x + \Delta t f \pi'_y \\ \pi'_y - \Delta t f \pi'_x \end{pmatrix}^{n+1}\right], \quad (25a)$$

$$W^{n+1} = \left[\frac{\alpha_w W - \Delta t g \tilde{\chi}/\chi^\circ}{\alpha_w + (\Delta t N)^2}\right]^n - \Delta t \frac{c_p (P\Theta)^\circ}{\alpha_w + (\Delta t N)^2} \pi_z'^{n+1}, \quad (25b)$$

with the local buoyancy frequency:

$$N = \sqrt{-g \frac{1}{\chi^\circ}\frac{d\overline{\chi}}{dz}}. \quad (26)$$

Insertion of the expressions in (25) into the pressure equation (24e) leads to a closed Helmholtz-type equation for π'^{n+1}:

$$\alpha_P \left(\frac{\partial P}{\partial \pi}\right)^\circ \pi'^{n+1} - \Delta t^2 \left\{ \left[\frac{c_p (P\Theta)^\circ}{1+(\Delta t f)^2}(\pi_x'^{n+1} + \Delta t f \pi_y'^{n+1})\right]_x + \left[\frac{c_p (P\Theta)^\circ}{1+(\Delta t f)^2}(\pi_y'^{n+1} - \Delta t f \pi_x'^{n+1})\right]_y + \left[\frac{c_p (P\Theta)^\circ}{\alpha_w + (\Delta t N)^2}\pi_z'^{n+1}\right]_z \right\} = R^n, \quad (27)$$

with the right-hand side:

$$R^n = \alpha_P \left(\frac{\partial P}{\partial \pi}\right)^\circ \pi'^n - \Delta t \left\{ \left[\frac{U^n + \Delta t f V^n}{1+(\Delta t f)^2}\right]_x + \left[\frac{V^n - \Delta t f U^n}{1+(\Delta t f)^2}\right]_y + \left[\frac{\alpha_w W^n - \Delta t g (\tilde{\chi}/\overline{\chi})^n}{\alpha_w + (\Delta t N)^2}\right]_z \right\}. \quad (28)$$

After its solution, backward reinsertion yields $(U, V, W, \tilde{\chi})^{n+1}$.

In all simulations shown in this paper, the Coriolis parameter is set to a constant, which eliminates the cross-derivative terms π'_{xy} from the elliptic operator in (27).

As evidenced by (24)–(28), the access to hydrostatic and pseudoincompressible dynamics is entirely encoded in the implicit Euler substeps of the scheme, marked by the appearance of the α_w and α_P parameters. In this paper we only demonstrate the behavior of the scheme for values of these parameters in {0, 1}, leaving explorations of a continuous blending of models with intermediate values of the parameters, as well as the development of an analogous switch to geostrophic limiting dynamics, to future work.

In appendix D we discuss how all substeps of the scheme can be reformulated equivalently in terms of full auxiliary variables χ and π instead of the perturbations χ', π' introduced above.

2) PRESSURE GRADIENT AND DIVERGENCE COMPUTATION IN THE GENERALIZED SOURCES

The linearized equations for inclusion of the source terms in (23a)–(23d) need to be evaluated at the cell centers when we apply the two steps of the trapezoidal rule in (17a) and (17c). To this end, the coefficients $(P\Theta)^\circ$ are evaluated at the cell centers as well, the linearization term from the equation of state $(\partial P/\partial \pi)^\circ$ is interpolated from the cell centers to the nodes according to

$$a_{i+1/2,j+1/2,k+1/2} = \frac{1}{8}\sum_{\lambda,\mu,\nu=0}^{1} a_{i+\lambda,j+\mu,k+\nu}, \quad (29)$$

and in a similar way from nodes to cell centers (Fig. 2a), and the components of the pressure gradient are approximated as

$$(\pi'_x)_{i,j,k} = \frac{1}{\Delta x}\left(\widehat{\pi}'_{i+\frac{1}{2},j,k} - \widehat{\pi}'_{i-\frac{1}{2},j,k}\right), \quad (30a)$$

with

$$\widehat{\pi}'_{i+\frac{1}{2},j,k} = \frac{1}{4}\left(\pi'_{i+\frac{1}{2},j+\frac{1}{2},k+\frac{1}{2}} + \pi'_{i+\frac{1}{2},j-\frac{1}{2},k+\frac{1}{2}} + \pi'_{i+\frac{1}{2},j+\frac{1}{2},k-\frac{1}{2}} + \pi'_{i+\frac{1}{2},j-\frac{1}{2},k-\frac{1}{2}}\right). \quad (30b)$$

Analogous formulae hold for the other Cartesian directions. The node-centered flux divergence in (24e) is formed on the basis of the cell-centered components of $\mathbf{V} = (U, V, W)$, using

$$(U_x)_{i+\frac{1}{2},j+\frac{1}{2},k+\frac{1}{2}} = \frac{1}{\Delta x}\left(\widehat{U}_{i+1,j+\frac{1}{2},k+\frac{1}{2}} - \widehat{U}_{i,j+\frac{1}{2},k+\frac{1}{2}}\right), \quad (31a)$$

$$\widehat{U}_{i,j+\frac{1}{2},k+\frac{1}{2}} = \frac{1}{4}(U_{i,j+1,k+1} + U_{i,j,k+1} + U_{i,j+1,k} + U_{i,j,k}), \quad (31b)$$

and analogous formulae for the other Cartesian directions (Fig. 2b).

These spatial discretizations inserted into the temporal semidiscretization of the implicit Euler step in (24)

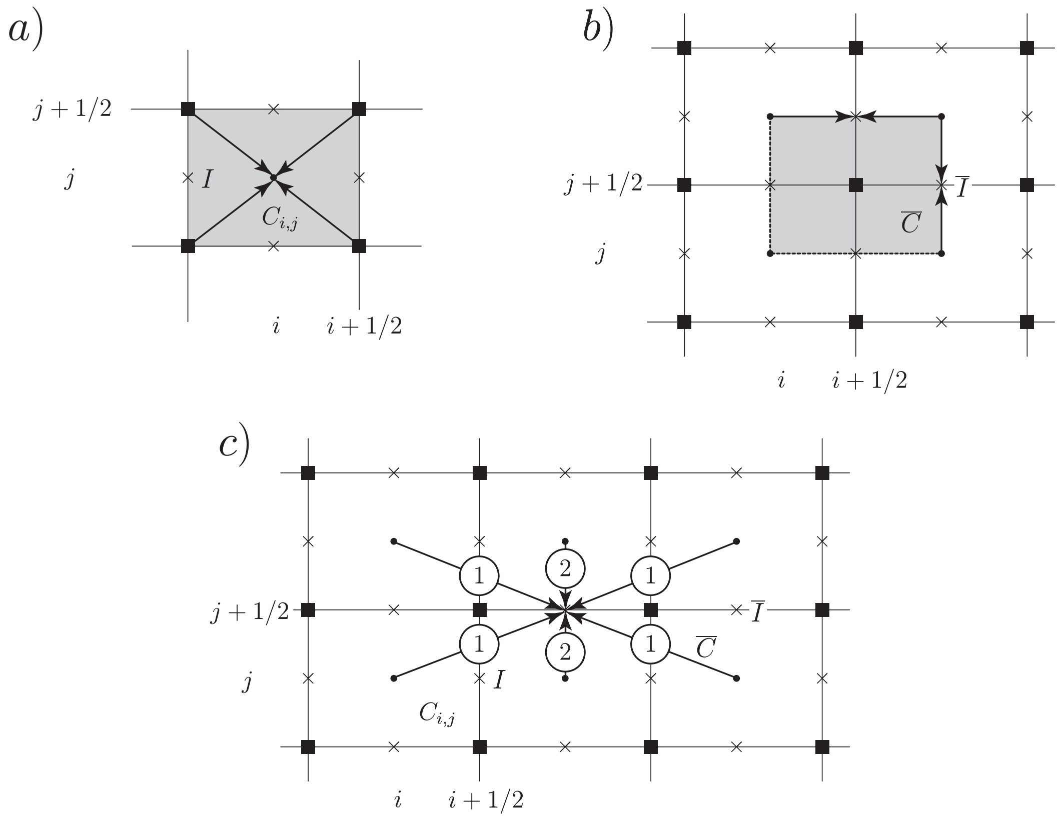

FIG. 2. Averaging patterns used in constructing fluxes and cell-centered divergences: (a) node-to-cell and analogous cell-to-node averages as in, respectively, (29) and (33); (b) cell-centered values of flux components (U, V, W) get averaged to the face centers of dual cells in (31); and (c) components of $P\mathbf{v}$ that are divergence-controlled relative to the nodes are averaged in a particular fashion to cell faces so as to exactly maintain the divergence control. In (a) and (b) all arrows carry the same weights, so we carry out simple arithmetic averages. In (c) the numbers in circles indicate relative weights of the participating cell-centered values in forming a face value.

lead to a node-centered discretization of the pressure Helmholtz equation based on nine-point and 27-point stencils of the Laplacian in two and three dimensions, respectively. The solution provides the required update of the node-centered perturbation pressure field and allows us to compute divergence-controlled cell-centered momenta. We note that in the case of the pseudoincompressible model, $\alpha_P = 0$, this amounts to a node-centered *exact* projection with a difference approximation that does allow for a checkerboard mode in case that the grid has equal spacing in all directions. Vater and Klein (2009) proposed a node-based exact projection that is free of such modes, but all tests in the present work used the simpler scheme described above.

3) DIVERGENCE CONTROLLED ADVECTIVE FLUXES VIA (15)

Advection is discretized using standard cell-centered flux divergences. Thus, the divergence of, for example, the vector field $\mathbf{V} = (U, V, W)$ uses the discrete approximation:

$$(\widetilde{U_x})_{i,j,k} = \frac{1}{\Delta x}\left(U_{i+\frac{1}{2},j,k} - U_{i-\frac{1}{2},j,k}\right), \tag{32}$$

and analogous expressions for V_y and W_z. For stability reasons, we need advective fluxes that are divergence-controlled in the sense that they are compatible with the Exner pressure evolution (24e). Yet, the Exner pressure is stored on grid nodes, so that the flux divergence on the right-hand side of (24e) is node-centered but not cell-centered. However, a simple node-to-cell average (Fig. 2a):

$$a_{i,j,k} = \frac{1}{8}\sum_{\lambda,\mu,\nu=0}^{1} a_{i-\frac{1}{2}+\lambda,j-\frac{1}{2}+\mu,k-\frac{1}{2}+\nu}, \tag{33}$$

yields a second-order accurate approximation to the cell average. This amounts to approximating the cell-centered divergence by the average of the adjacent node-centered divergences. It turns out that this is also equivalent to determining the cell-face advective fluxes from the interpolation formula:

$$U_{i+\frac{1}{2},j,k} = \frac{1}{2}\left(\widehat{\hat{U}}_{i+1,j,k} + \widehat{\hat{U}}_{i,j,k}\right), \tag{34a}$$

$$\widehat{\hat{U}}_{i,j,k} = \frac{1}{4}\sum_{\mu,\nu=0}^{1} \hat{U}_{i,j-\frac{1}{2}+\mu,k-\frac{1}{2}+\nu}, \tag{34b}$$

with the $\hat{U}$ taken from (31b), and with analogous expressions for the other Cartesian directions. The resulting effective averaging formula takes cell centered components of $P\mathbf{v}$ and generates cell face normal transport fluxes (see Fig. 2c for a two-dimensional depiction).

By this approach, we remove the necessity of separately controlling the advective fluxes across the cell faces by a cell-centered elliptic solve (MAC-projection) on the one hand and controlling the divergence of the cell-centered velocities by another elliptic equation for nodal pressures on the other hand, as in, e.g., Bell et al. (1989); Almgren et al. (2006); Schneider et al. (1999); Benacchio et al. (2014). Thus, the present scheme works with the node-based discretization of the Helmholtz equation only. We note in passing that this approach requires an *exact* projection for the nodal divergence.

d. *Synchronization of auxiliary variables*

The proposed scheme achieves large time step capabilities by introducing two additional auxiliary variables, π' and χ' (or π, χ in the full variable variant) that enable the linearization used in formulating the implicit part of the scheme. As described in this section, the buoyancy variable, χ', is synchronized with $\chi = 1/\Theta = \rho/P$ at the beginning of each time step, whereas the pressure variable, π', is evolved redundantly relative to the cell-centered variable P.

1) ADJUSTMENT OF THE POTENTIAL TEMPERATURE PERTURBATION

The advection of inverse potential temperature, $\chi = \rho/P$, is realized through the conservative updates of ρ and P according to (17b) and (17d). Thus it is completed after the advection step and unaffected by the final implicit Euler step of (17c).

Instead, the perturbation χ' undergoes three advances. The first advance occurs in the explicit Euler step (17a) for the linearized perturbation equation (23d), the second in the advection step, and the third in the final implicit Euler step (17c). The explicit Euler and implicit Euler steps discretize the linearized perturbation equation (23d) by evaluating both $\tilde{\chi}$ and W at the cell centers. This is a nonconservative discretization of the advection of the background distribution, and thus it cannot be equivalent to the conservative updates for the full variable χ described above. However, discrepancies between χ and χ' cannot accumulate over many time steps, because at the beginning of each time step we reset $(\chi')^n = \chi^n - (\overline{\chi})^n$.

2) SYNCHRONIZATION OF NODAL AND CELL PRESSURES

In section 4c(3) we constructed the cell-centered advective flux divergence from the arithmetic average of the divergences obtained on the adjacent nodes. By the same reasoning the cell-centered update of P that results from these cell-centered divergences corresponds to the node-to-cell average (33) for $(\partial P/\partial \pi)^{\circ}(\pi^{n+1} - \pi^n)$. If, in addition, the pressure Helmholtz equation from (27) is solved with an outer iteration such that after convergence this coefficient is approximated by

$$\left(\frac{\partial P}{\partial \pi}\right)^{\circ}_{i+\frac{1}{2},j+\frac{1}{2},k+\frac{1}{2}} = \left(\frac{P^{n+1} - P^n}{\pi^{n+1} - \pi^n}\right)_{i+\frac{1}{2},j+\frac{1}{2},k+\frac{1}{2}}, \tag{35}$$

then the cell-centered time updates of P could be guaranteed to always equal the node-to-cell average of their nodal counterparts as computed from the first implicit Euler in (15) by doubling the resulting Exner pressure update according to the implicit midpoint rule. However, in all tests shown below, the nodal pressure was computed from the implicit trapezoidal update (17), so that the cell-centered P and the nodal π' are evolved separately in the present implementation. In some cases we found small differences between the two variables. Also in view of the lack of feedback of these differences onto the dynamics, we deem them acceptable at this stage, and we propose avenues of development in the discussion.

5. Numerical results

The algorithm described in the previous sections was tested on a suite of benchmarks of dry compressible dynamics on a vertical $x - z$ slice at various scales. The suite draws on the set of Benacchio (2014); Benacchio et al. (2014) including a cold air bubble and nonhydrostatic inertia–gravity waves, and adds three larger-scale configurations for the gravity waves, with the aim to validate the robustness and accuracy of the new buoyancy-implicit strategy, and the scheme's capability of accessing compressible, pseudoincompressible, and hydrostatic dynamics. For the cold air bubble, we also show the results obtained with a full variable approach. We remark that the present paper does not focus on efficiency. While the coding framework is 3D ready, we leave parallelization and performance on three-dimensional tests for future work. The scheme is implemented in plain C language and uses the BiCGSTAB linear solver (Van der Vorst 1992) for the solution of the elliptic problems. The solver tolerance was set at Res $[(24e)/\Delta t] \leq 10^{-8}$ throughout, where Res$(\cdot)$ denotes the residual in the iterative solution of the equation in the argument. Thus we are controlling the accuracy of the advective flux divergence $U_x + V_y + W_z$. We also define the advective Courant number as follows:

$$\mathrm{CFL}_{\mathrm{adv}} = \max_{i \in \{1,2,3\}} \left(\frac{\Delta t v_i}{\Delta x_i} \right), \tag{36}$$

where v_i are the components of the velocity, Δx_i the grid spacing in the i direction, and the acoustic Courant number as follows:

$$\mathrm{CFL}_{\mathrm{ac}} = \max_{i \in \{1,2,3\}} \left[\frac{\Delta t (v_i + c)}{\Delta x_i} \right], \tag{37}$$

where $c = \sqrt{\gamma R T}$ denotes the speed of sound. Finally, while we are aware that a B-grid-like setting allows for computational modes, we did not observe spurious oscillations in code validations based on the results in rotating vortex tests of Kadioglu et al. (2008) [not shown, see also Benacchio et al. (2014)].

a. Density current

The first test case, proposed by Straka et al. (1993), concerns the simulation of a falling bubble of cold air in a neutrally stratified atmosphere $(x, z) \in [-25.6, 25.6] \times [0, 6.4]\,\mathrm{km}^2$. The reference potential temperature and pressure are $\theta_{\mathrm{ref}} = 300\,\mathrm{K}$ and $p_{\mathrm{ref}} = 10^5\,\mathrm{Pa}$, the thermal perturbation is

$$T' = \begin{cases} 0\,\mathrm{K} & \text{if} \quad r > 1 \\ -15[1 + \cos(\pi r)]/2\,\mathrm{K} & \text{if} \quad r < 1 \end{cases}, \tag{38}$$

where $r = \{[(x - x_c)/x_r]^2 + [(z - z_c)/z_r]^2\}^{0.5}$, $x_c = 0$, $x_r = 4$, $z_c = 3$, and $z_r = 2\,\mathrm{km}$. Boundary conditions are solid walls on top and bottom boundaries and periodic elsewhere. To obtain a converged solution, artificial diffusion terms $\rho\mu\nabla^2\mathbf{u}$ and $\rho\mu\nabla^2\boldsymbol{\Theta}$ are added to the momentum and P equations, respectively, with $\mu = 75\,\mathrm{m}^2\,\mathrm{s}^{-1}$. The terms are nonstiff, discretized by the explicit Euler method individually, and tied into the scheme via operator splitting just before the second backward Euler step (17c).

In the reference setup for this case, the buoyancy-implicit model is run at a resolution $\Delta x = \Delta z = 50\,\mathrm{m}$ with time step chosen according to the minimum of $\Delta t_{\mathrm{fix}} = 4\,\mathrm{s} \times \Delta x/50\,\mathrm{m}$ and a time step based on the advective Courant number $\mathrm{CFL}_{\mathrm{adv}} = 0.96$. Driven by its negative buoyancy, the initial perturbation moves downward, impacts the bottom boundary and travels sideways developing vortices (Fig. 3, left column and top right panel). The numerical solution converges with increasing spatial resolution (Fig. 4), and the final perturbation amplitude and front position agree with published results [Table 1, for comparison see, e.g., Giraldo and Restelli (2008) and the similar table in Melvin et al. (2019)]. The final minimum potential temperature perturbation at 25 m resolution agrees with the result in Melvin et al. (2019) up to the third decimal digit. A run operated with full variables yields alike solution quality to runs operated with perturbations (Fig. 3, middle right panel and bottom right panel). The difference is of the order of $10^{-5}\,\mathrm{K}$ and the relative L^2 error is 2.33×10^{-4}, giving an empirical confirmation of the close proximity of the two approaches.

b. Inertia–gravity waves

The next set of tests consists of gravity waves in a stably stratified channel with constant buoyancy frequency $N = 0.01\,\mathrm{s}^{-1}$, $\theta(z = 0) = 300\,\mathrm{K}$, horizontal extension $x \in [0, x_N]$, and vertical extension $z = 10\,\mathrm{km}$, proposed by Skamarock and Klemp (1994). The thermal perturbation is

$$\theta'(x, z, 0) = 0.01\,\mathrm{K} \times \frac{\sin(\pi z/H)}{1 + [(x - x_c)/a]^2}, \tag{39}$$

with $H = 10\,\mathrm{km}$, $x_c = 100\,\mathrm{km}$, $a = x_N/60$, and there is a background horizontal flow $u = 20\,\mathrm{m\,s}^{-1}$. We consider three configurations for the horizontal extension $x_N = 300$, 6000, 48 000 km, with respective final times $T = 3000$, 60 000, 480 000 s. The first two configurations correspond respectively to the nonhydrostatic case and the hydrostatic case of Skamarock and Klemp (1994), the third planetary-scale configuration is introduced in this paper. In all configurations, the buoyancy-implicit model is run with 300×10 cells, as in Skamarock and Klemp (1994), and $\mathrm{CFL}_{\mathrm{adv}} = 0.9$.

In the first configuration, the initial perturbation spreads out onto gravity waves driven by the underlying buoyancy stratification (Fig. 5). In the second configuration, run with rotation (Coriolis parameter value $f = 10^{-4}\,\mathrm{s}^{-1}$), a geostrophic mode is also present in the center of the domain (Fig. 6). In both cases, the values obtained by running the compressible model (COMP) closely resemble published results in the literature including, for the nonhydrostatic case, the buoyancy-explicit compressible result in Benacchio et al. (2014). At $\mathrm{CFL}_{\mathrm{adv}} = 0.9$, the time step used in the first configuration is $\Delta t \approx 44.83\,\mathrm{s}$,

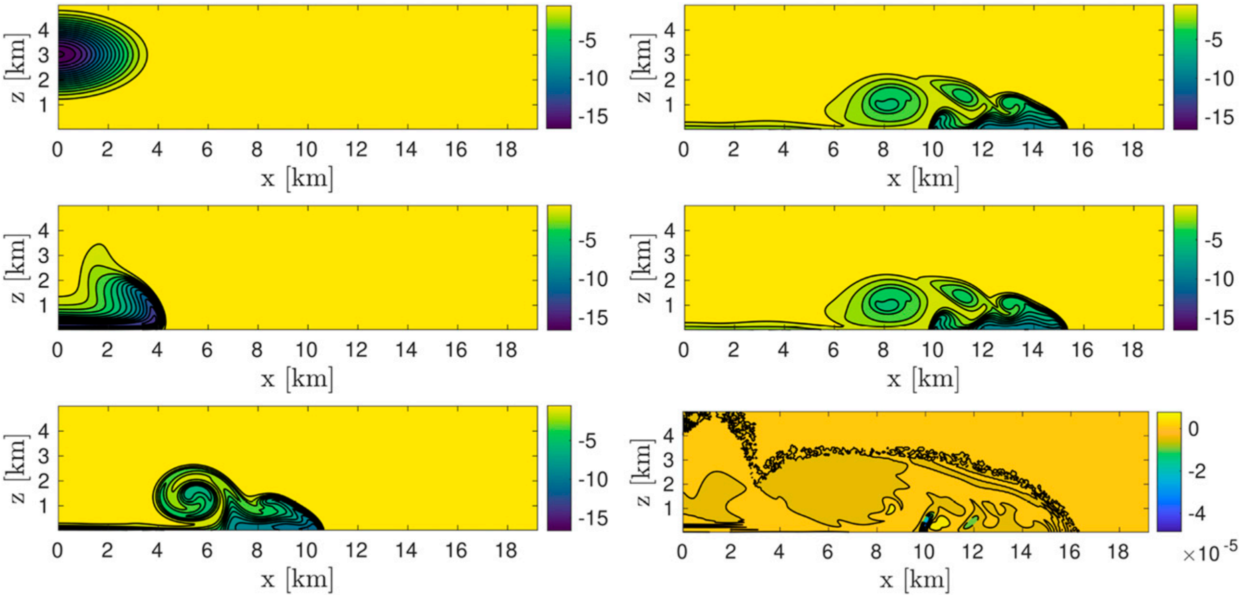

FIG. 3. Density current test case at spatial resolution $\Delta x = \Delta z = 50$ m, $\mathrm{CFL_{adv}} = 0.96$. (left) Potential temperature perturbation at (from top to bottom) $t = 0, 300, 600$ s, run with perturbation variables. (right) Potential temperature perturbation at final time $t = 900$ s, run with (top) perturbation variables and (middle) full variables. Contours in the range $[-16.5, -0.5]$ K with a 1 K contour interval. (bottom right) Difference between the top right plot and the middle right plot, contours in the range $[-4.5, 0.5] \times 10^{-5}$ K with a 0.5×10^{-6} K contour interval.

a 12 times larger value than Benacchio et al. (2014)'s 3.75 s. The time step value used here is also in line with Melvin et al. (2019), who ran the configuration with $\Delta t = 12$ s at buoyancy-implicit CFL $= 0.3$. For the second configuration at $\mathrm{CFL_{adv}} = 0.9$, the time step used is $\Delta t \approx 896.48$ s, equivalent to an acoustic $\mathrm{CFL_{ac}} \approx 309.5$ and $N\Delta t = 8.96$.

The third new planetary-scale configuration is run without rotation to suppress the otherwise dominant geostrophic mode and highlight the wave dynamics. At final time $T = 480\,000$ s ($\approx$5.5 days), the solution quality with the compressible model is good in terms of symmetry, absence of oscillations, and final position of the outermost crests (Fig. 7). Note also the structural similarity of the result for this configuration with the nonhydrostatic test run with the hydrostatic setup. The time step in this run at $\mathrm{CFL_{adv}} = 0.9$ is $\Delta t \approx 7100$ s, equivalent to $N\Delta t \approx 71$ and to an acoustic $\mathrm{CFL_{ac}} \approx 2.4 \times 10^3$.

For all configurations, we report the pseudoincompressible (PI) result obtained using $\alpha_P = 0$, that is, by switching off compressibility zeroing the diagonal term in the Helmholtz equation, and the hydrostatic (HY) result obtained using $\alpha_w = 0$, that is, by zeroing the dynamic tendency of the velocity in the vertical momentum equation (middle panels of Figs. 5–7), and plot the differences with the compressible result, COMP–PI and COMP–HY (bottom panels of Figs. 5–7). For the nonhydrostatic test, as already found with the earlier implementation of the model in Benacchio et al. (2014), the PI result is very close to the COMP result. The hydrostatic configuration fails to capture the central wave features, and the COMP–HY discrepancy is larger by an order of magnitude than the COMP–PI discrepancy. The situation is reversed for the hydrostatic test and the planetary test where the COMP–HY difference is smaller than the COMP–PI difference. Moreover, the COMP–PI difference gets larger, and the COMP–HY difference smaller, for larger horizontal scales, as expected with smaller vertical-to-horizontal domain size aspect ratios.

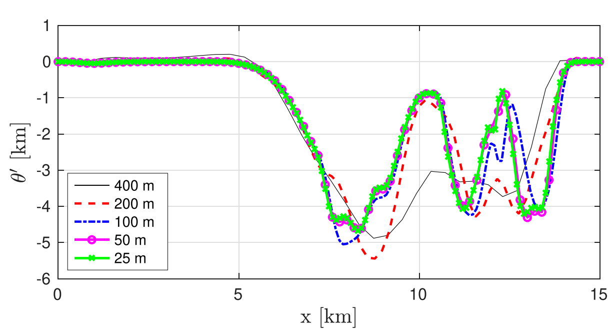

FIG. 4. One-dimensional cut at height $z = 1200$ m for the potential temperature perturbation at final time $t = 900$ s in the density current test case run with $\mathrm{CFL_{adv}} = 0.96$. Spatial resolutions $\Delta x = \Delta z = 400$ m (black solid), 200 m (red dashed), 100 m (blue dashed-dotted), 50 m (magenta solid, circles), 25 m (green solid, crosses).

TABLE 1. Minimum and maximum potential temperature perturbation and front location (rightmost intersection of -1 K contour with $z = 0$) for the density current test at several resolution values.

Grid size (m)	θ'_{min} (K)	θ'_{max} (K)	Front location (m)
400	-8.1483	0.2684	14 125
200	-8.9377	0.2299	14 884
100	-9.2168	0.1789	15 199
50	-9.5056	0.0906	15 325
25	-9.6577	0.0037	15 380

c. Superposition of acoustic–gravity waves and inertia–gravity waves

As final corroboration of the properties of the model, the hydrostatic configuration is rerun with a different value of the Coriolis parameter $f = 1.031\,26 \times 10^{-4}\,\mathrm{s}^{-1}$, initial temperature $T(z = 0) = 250\,\mathrm{K}$, isothermal background distribution, and no background flow. A time step of $\Delta t = 0.5\,\mathrm{s}$ is used for a run with 1200×80 cells as in Baldauf and Brdar (2013).

The initial data trigger a rapidly oscillating vertical acoustic–gravity wave pulse that is followed over more than 230 000 time steps without decay and with small horizontal spread. Superimposed is a longer wavelength internal wave mode that sends two pulses sideways from the center of the initial perturbation, leaving the oscillating acoustic gravity mode behind. Results with the buoyancy-implicit model display good symmetry (Fig. 8, top three panels) and compare well with the reference [Fig. 4 in Baldauf and Brdar (2013)]. The multiscale nature of the case is evident in particular in the plot of the vertical velocity. The results obtained with the present scheme are superior to those generated by the COSMO dynamical core in its production setting with a stabilizing time offset of $\theta = 0.7$ for the vertically implicit linear acoustic mode. With their off-centered setting, the rapid vertical acoustic oscillations get damped away rapidly and are absent from their final output [Fig. 6 in Baldauf and Brdar (2013)]. However, the COSMO code run with no time offset, $\theta = 0.5$, for second order accuracy does maintain the vertical acoustics over the entire time period [Fig. 5 in Baldauf and Brdar (2013)], and it represents the very slow horizontal spreading of this mode somewhat more accurately than our scheme. A snapshot taken 520 time steps before completion of our

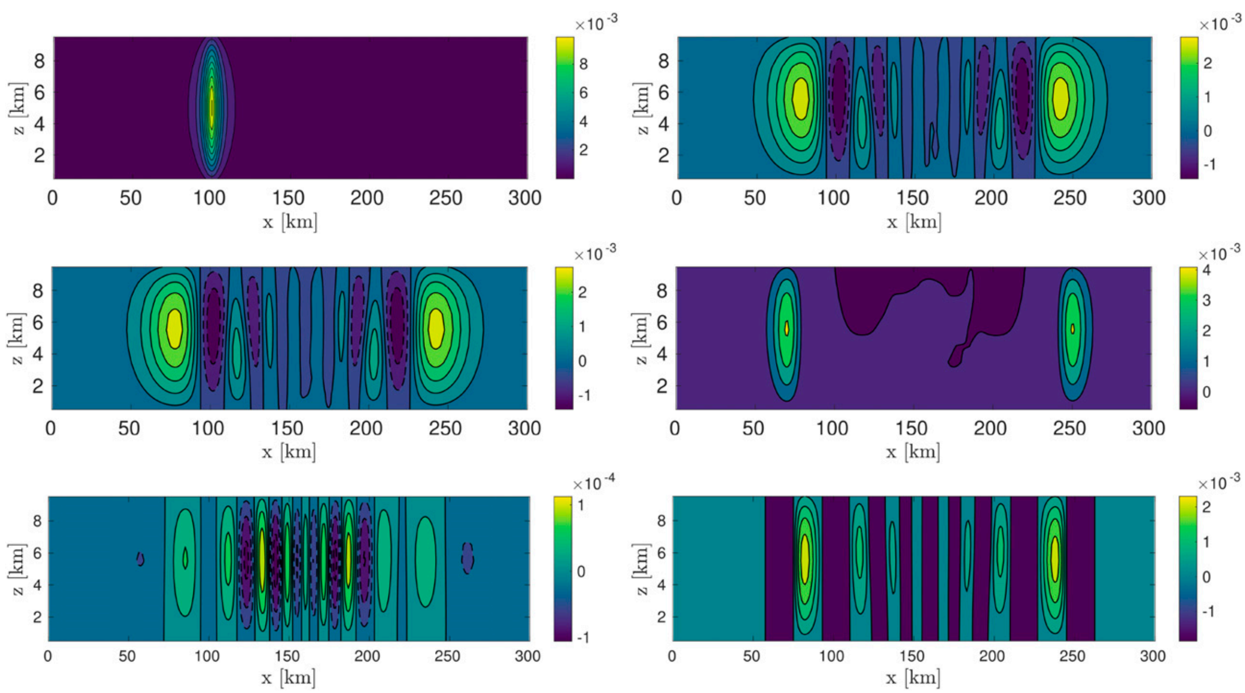

FIG. 5. Potential temperature perturbation for the nonhydrostatic inertia–gravity wave test from Skamarock and Klemp (1994), $\Delta x = \Delta z = 1$ km, $\mathrm{CFL_{adv}} = 0.9$. (top left) Initial data (contours in the range [0, 0.01] K with a 0.001 K interval) and computed value at final time $T = 3000$ s in (top right) compressible mode, (middle left) pseudoincompressible mode, and (middle right) hydrostatic mode. Contours are in the range $[-0.0025, 0.0025]$ K with a 0.0005 K interval for the nonhydrostatic plots, in the range $[-0.005, 0.005]$ K with a 0.001 K interval for the hydrostatic plot. (bottom) (left) Difference between the compressible run and the pseudoincompressible run and (right) between the compressible run and the hydrostatic run. In the left panels, contours in the range $[-2.5, 2.5] \times 10^{-4}$ K with a 5×10^{-5} K interval, and in the right panels $[-5, 5] \times 10^{-5}$ K with a 10^{-5} K interval. Negative contours are dashed.

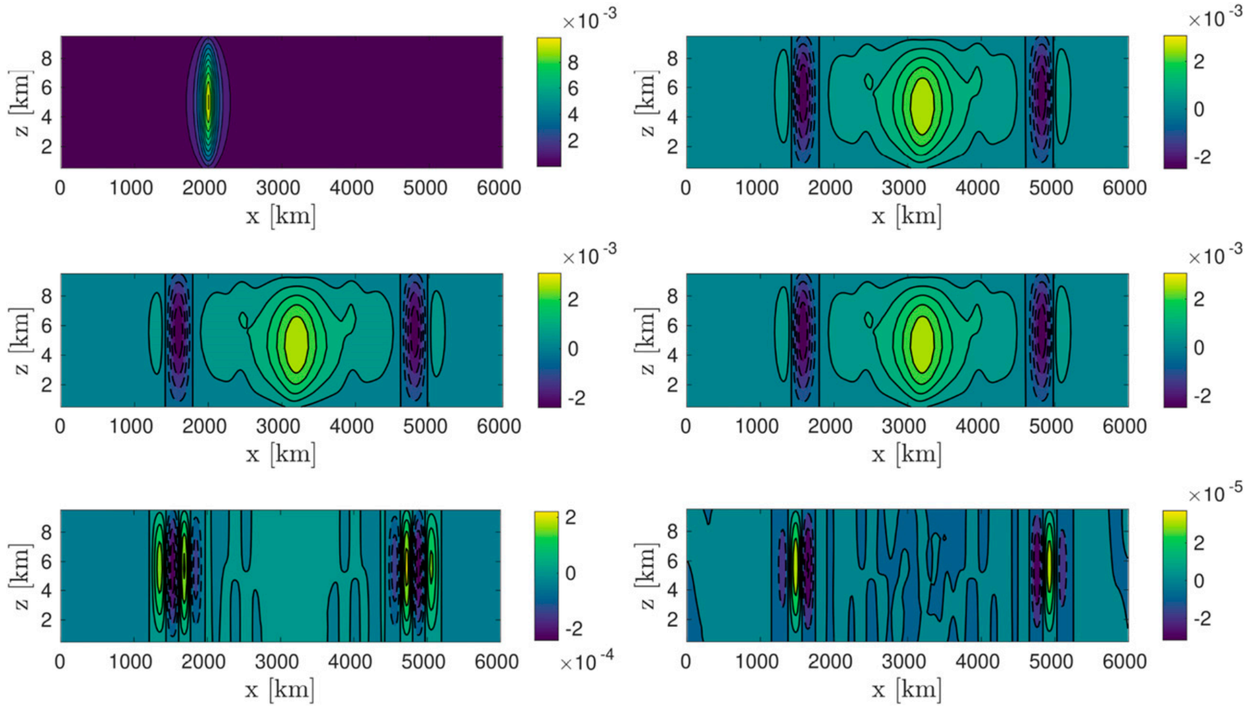

FIG. 6. Potential temperature perturbation for the hydrostatic inertia–gravity wave test from Skamarock and Klemp (1994), $\Delta x = 20$ km, $\Delta z = 1$ km, $\mathrm{CFL}_{\mathrm{adv}} = 0.9$. (top left) Initial data and computed value at final time $T = 60\,000$ s in (top right) compressible mode, (middle left) pseudoincompressible mode, and (middle right) hydrostatic mode. Contours as in Fig. 5. (bottom) (left) Difference between the compressible run and the pseudoincompressible run and (right) between the compressible run and the hydrostatic run. In the left panels contours in the range $[-2.5, 2.5] \times 10^{-4}$ K with a 5×10^{-5} K interval, and in the right panels $[-5, 5] \times 10^{-5}$ K with a 10^{-5} K interval. Negative contours are dashed.

model simulation shows better agreement in the maximum amplitude with the reference in terms of maximum vertical velocity (Fig. 8, bottom panel).

6. Discussion and conclusions

This paper extended a semi-implicit numerical model for the simulation of atmospheric flows to a scheme with time step unconstrained by the internal wave speed and without subtraction of a background state from the primary prognostic variables. The conservative, second-order accurate finite volume discretization of the rotating compressible equations evolves cell-centered variables through a three-stage procedure, made of an implicit midpoint rule step, an advection step, and an implicit trapezoidal step. By design the model agrees with the pseudoincompressible system in the small-scale vanishing Mach number limit and with the hydrostatic system in the large-scale limit. Moreover, the discretization is designed so it can straightforwardly be switched to strictly solving either of these two limiting systems. The modeling framework features the option of running the scheme in a variant that avoids perturbation variables entirely for the formulation of the implicit problem. Numerical solutions with and without the option were tested for close similarity.

The compressible scheme was applied to a suite of benchmarks of atmospheric dynamics at different scales. Compared with the previous variant of the model in Benacchio (2014); Benacchio et al. (2014), who used a buoyancy-explicit discretization, the present scheme achieves comparable accuracy, competitive solution quality, and absence of oscillations with much larger time steps for the cases under gravity. New compressible simulations of the hydrostatic-scale inertia–gravity wave tests of Skamarock and Klemp (1994) demonstrated the large time step capability of the buoyancy-implicit numerical scheme. A more challenging planetary-scale version of this class of tests was introduced in this paper and revealed the robustness of the discretization for 2-h-long time steps. The authors are unaware of published attempts to run the test at this scale.

An additional test by Baldauf and Brdar (2013), geared toward revealing the long-time simulation stability and energy perservation of the scheme, yielded results comparable to those obtained with

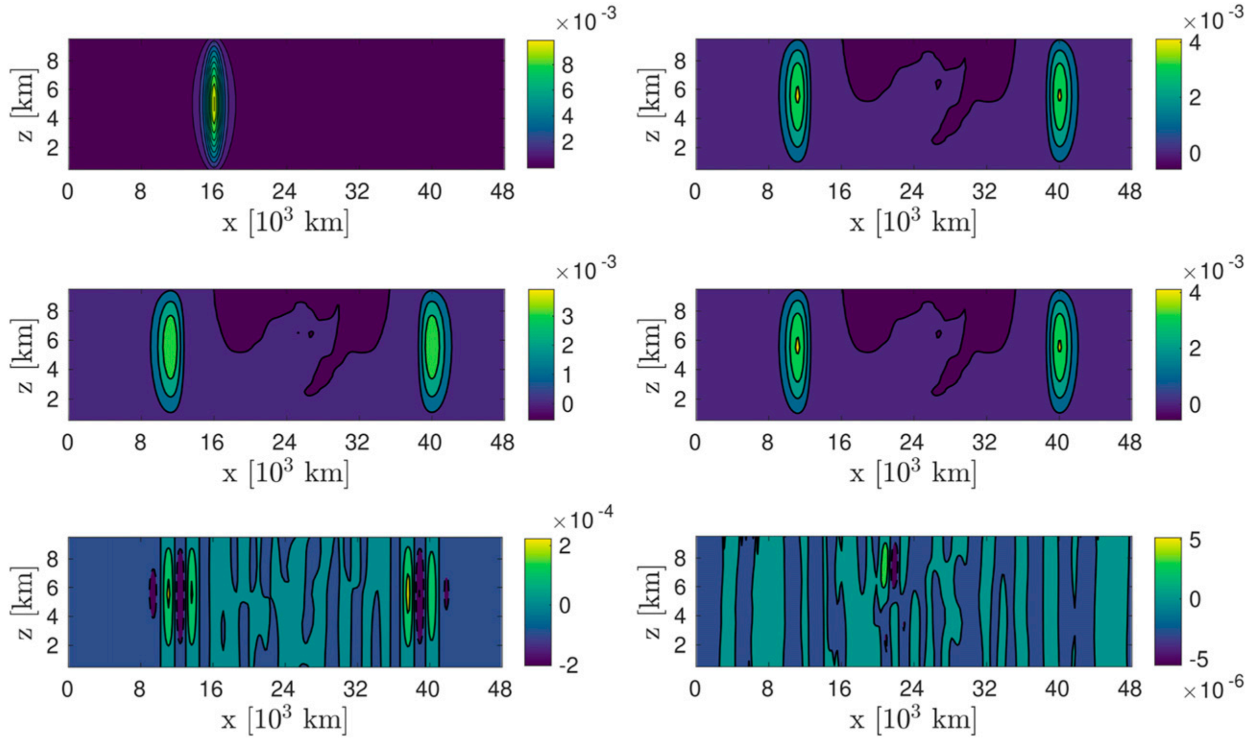

FIG. 7. Potential temperature perturbation for the planetary-scale gravity wave test, $\Delta x = 160$ km, $\Delta z = 1$ km, $\mathrm{CFL_{adv}} = 0.9$. (top left) Initial data (contours as in Figs. 5–6) and computed value at final time $T = 480\,000$ s in (top right) compressible mode, (middle left) pseudoincompressible mode, and (middle right) hydrostatic mode. Contours in the range $[-0.005, 0.005]$ K with a 0.001 K interval. (bottom) (left) Difference between the compressible run and the pseudoincompressible run and (right) between the compressible run and the hydrostatic run. In the left panels contours in the range $[-4, 6] \times 10^{-4}$ K with a 10^{-4} K interval, and in the right panels $[-1.5, 1.5] \times 10^{-5}$ K with a 3×10^{-6} K interval. Negative contours are dashed.

the reference's higher-order discontinuous Galerkin scheme, albeit with somewhat less of a spreading of the oscillatory mode.

Furthermore, the nonhydrostatic-, hydrostatic-, and new planetary-scale setups of the gravity wave test were run both in pseudoincompressible mode and in hydrostatic mode, thereby extending the switching capability previously shown in Benacchio et al. (2014) for the pseudoincompressible-to-compressible configurations. With increasingly large scales, differences with the compressible runs increased for the pseudoincompressible runs and decreased for the hydrostatic runs as expected, with the reverse trend for decreasing scales.

The results presented here suggest several avenues of development in a number of areas. First, the scheme serves as the starting point for implementing the multimodel theoretical framework of Klein and Benacchio (2016), which aims to achieve balanced initialization and data assimilation at all scales by smoothly blending between different operation modes. As proposed by Benacchio et al. (2014), such a multimodel discretization could be run with reduced soundproof or hydrostatic dynamics during the first time steps after setup or assimilation, then resorting to the fully compressible model for the transient sections. The development in the present work yields hydrostasy at large scale as well as pseudoincompressibility at small scales as the accessible asymptotic dynamics in the blended scheme. The discretization could then be applied to run tests in spherical geometry, with the ultimate aim of comparing with existing schemes used in numerical weather prediction research and operations.

Future tests will necessarily involve a detailed analysis of efficiency and computational cost of the present model. The Helmholtz solve described above works with a nine-point stencil in two dimensions (27-point in three dimensions). While results on the density current test closely agree with those of Melvin et al. (2019) and Melvin et al. (2010)—whose operational version uses a seven-point stencil in three dimensions—further work is needed to demonstrate that the scheme has an effective resolution as high as a C-grid scheme, and that the implicit solve is as efficient.

Concerning the discretization of the equation of state, the implicit midpoint rule that is used in (16)

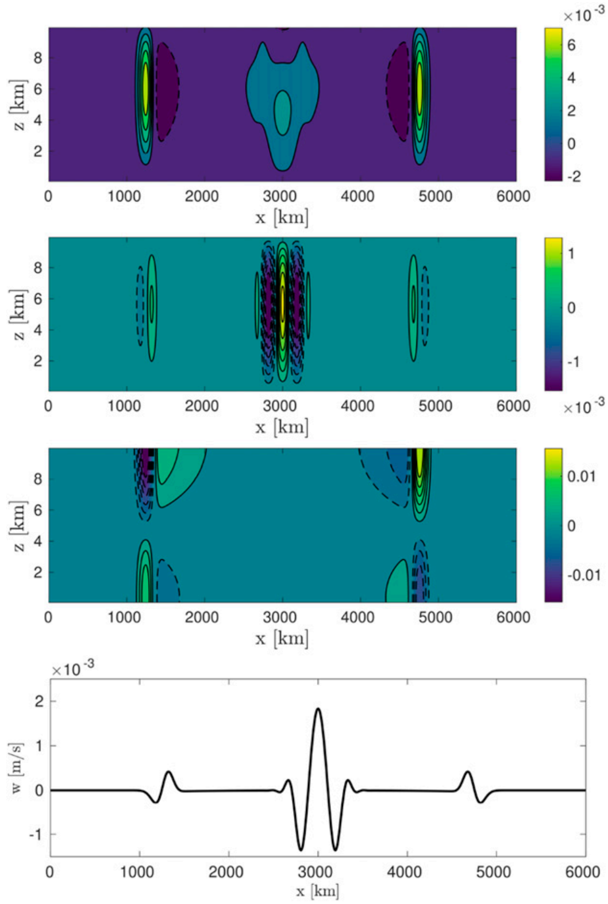

FIG. 8. (from top to bottom) Temperature perturbation, vertical velocity, horizontal velocity at final time $T = 28\,800$ s, and a one-dimensional cut of vertical velocity through $z = 5$ km at time $T = 28\,540$ s for the inertia–gravity wave test with rotation of Baldauf and Brdar (2013), $\Delta x = 5$ km, $\Delta z = 125$ m, $\Delta t = 0.5$ s. Initial perturbation as in Fig. 6 (top panel). Contours in the range $[-6, 6] \times 10^{-3}$ K with a 1.2×10^{-3} K interval in the top panel, $[-1.2, 1.2] \times 10^{-3}$ m s^{-1} with a 2×10^{-4} m s^{-1} interval (vertical velocity), $[-0.012, 0.012]$ m s^{-1} with a 2×10^{-3} m s^{-1} interval (horizontal velocity). Negative contours are dashed, zero contour not shown.

is symplectic. In principle, the linearization used here destroys this property. Yet, the remaining error in a time step is of the order of the pressure increment squared, and relative pressure increments in the tests performed above range from $O(10^{-4})$ for the density current test case to $O(10^{-8})$ for the planetary-scale gravity wave–much smaller than the truncation error associated with the numerical scheme, and close to the effective accuracy provided by double-precision calculations. It will be interesting to test the net influence of a nonlinear iteration on cases with larger pressure fluctuations in future work.

Finally, the redundancy of the Exner pressure maintained in the present scheme deserves further attention. One possible route forward would be to attempt an analytical proof that the cell-centered P and nodal π' cannot diverge from each other. Another would be the development of a robust synchronization strategy that overwrites the nodal pressure using the cell-centered data.

Acknowledgments. T.B. acknowledges funding by the ESCAPE-2 project, European Union's Horizon 2020 research and innovation program under Grant 800897. R.K. acknowledges funding by Deutsche Forschungsgemeinschaft through the Collaborative Research Center CRC 1114 "Scaling cascades in complex systems," project A02, and the support of the European Centre for Medium-Range Weather Forecasts under their ECMWF Fellow Program. Extensive discussions with Piotr Smolarkiewicz, Christian Kühnlein, and Nils Wedi have been crucial for the present developments. Nigel Wood, Golo Wimmer, and three anonymous reviewers are gratefully acknowledged for critical reads of the manuscript that have greatly contributed to improving its contents and presentation.

APPENDIX A

Second-Order Accuracy

To maintain second-order accuracy of the overall scheme, a first-order accurate time integration from the last completed time step at t^n is sufficient for generating the half-time level fluxes $(P\mathbf{v})^{n+1/2}$. This becomes transparent through a truncation error analysis for any equation of the form $\dot{y} = R(y, t)$. First we observe that

$$\frac{y(t^{n+1}) - y(t^n)}{\Delta t} = \dot{y}(t^{n+1/2}) + \mathscr{O}(\Delta t^2) \tag{A1}$$

by straightforward Taylor expansion. Then, for any first-order approximation, say $R^{n+1/2}$, to the right-hand side at the half-time level we have

$$\begin{aligned}\dot{y}(t^{n+1/2}) &= R[y(t^{n+1/2})] = R\left[y(t^n) + \frac{\Delta t}{2}\dot{y}(t^n) + \mathscr{O}(\Delta t^2)\right] \\ &= R^{n+1/2} + \mathscr{O}(\Delta t^2),\end{aligned} \tag{A2}$$

where $R^{n+1/2} = R[y(t^n) + (\Delta t/2)\dot{y}(t^n)]$ is the right-hand side evaluated at a state that is lifted from t^n to $t^{n+1/2}$ just by a first-order method. Reinserting into (A1) we find indeed

$$\frac{y(t^{n+1}) - y(t^n)}{\Delta t} = R^{n+1/2} + \mathscr{O}(\Delta t^2). \tag{A3}$$

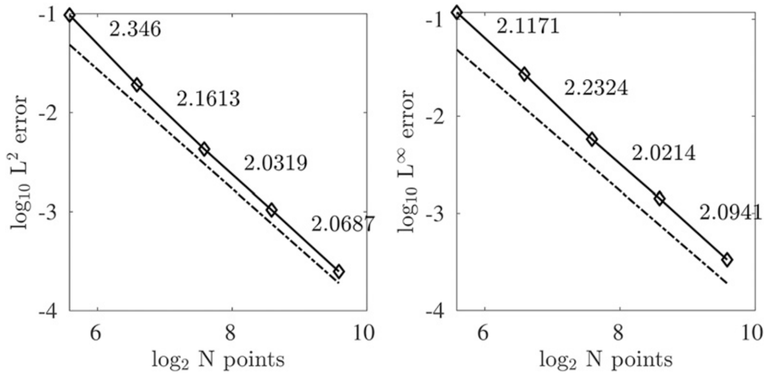

FIG. B1. Convergence story for the nodal pressure variable in the rotating traveling vortex case. Grid refinements from 48 × 48 to 768 × 768 points, error of the solution at time $T = 1$ s with respect to the initial data in the (left) L^2 norm and (right) L^∞ norm. The dashed–dotted line displays second-order convergence.

APPENDIX B

Pressure Convergence

To show that the model does not display oscillations or instabilities, we ran the case of a traveling rotating vortex in the doubly periodic domain $[0, 1]^2$ of Kadioglu et al. (2008). We refer to section 4a of Benacchio et al. (2014) for a description. Both density and pressure variables after one revolution of the vortex (at $T = 1$ s) are in good agreement with the initial data (not shown). In particular, the error on the nodal pressure at final time with respect to the initial data displays second-order convergence with increasing spatial resolution both in the L^2 and L^∞ norm (Fig. B1).

APPENDIX C

Preservation of Constant Values of Advected Scalars

The scheme can be shown analytically to preserve constant values of advected scalars. It is a very brief argument: Suppose q is advected by $(P\mathbf{v})$, so that

$$(Pq)_t + \nabla \cdot (P\mathbf{v}q) = 0, \tag{C1}$$

$$P_t + \nabla \cdot (P\mathbf{v}) = 0, \tag{C2}$$

and the initial data have $q(0, x) = q_0 =$ const. By construction of the MUSCL advection scheme, which reconstructs the advected quantities (i.e., q in the present case), all slopes for q will be discretely zero, and therefore discretely (i.e., with ∇ replaced by $\widetilde{\nabla}$):

$$\widetilde{\nabla} \cdot (P\mathbf{v}q)^{n+1/2} = q_0 \widetilde{\nabla} \cdot (P\mathbf{v})^{n+1/2}. \tag{C3}$$

Next, as a consequence,

$$(Pq)^{n+1} - (Pq)^n = q_0(P^{n+1} - P^n) \Rightarrow$$
$$q^{n+1} = (Pq)^{n+1}/P^{n+1} \equiv q_0. \tag{C4}$$

APPENDIX D

Full Variable Formulation

Here we demonstrate that the semi-implicit formulation of our scheme in terms of perturbation variables χ', π' has an analytically equivalent form in terms of full variables. The central expression in this context is the combination of the vertical pressure gradient and buoyancy terms in (1c). Multiplying it by P/ρ, and recalling that $P = \rho\Theta$, we obtain the form needed in the explicit and implicit Euler steps of the scheme:

$$\frac{P}{\rho}(c_p \rho \Theta \pi_z + \rho g) = (P\Theta)(c_p \pi_z + g\chi) = (P\Theta)(c_p \pi'_z + g\chi')$$
$$= c_p (P\Theta)\pi'_z + g\tilde{\chi}/\chi. \tag{D1}$$

Here we have used that $c_p \overline{\pi}_z = -g\overline{\chi}$ by (8) to shift from full to perturbation variables, and $P\chi' = \tilde{\chi}$ by the definition right after (23). It follows that with the particular use of the current state quantities $(P\Theta)^\circ$ and $\chi^\circ = 1/\Theta^\circ$ in the formulation of the implicit Euler step in (24), we can always trivially add and subtract the background state distributions $\overline{\pi}_z$ and $\overline{\chi}$ to the perturbations π'_z and χ' without changing the result at the analytical level:

$$c_p (P\Theta)^\circ \pi_z'^{n+1} + g\tilde{\chi}^{n+1}/\chi^\circ = (P\Theta)^\circ (c_p \pi_z'^{n+1} + g\chi'^{n+1})$$
$$= (P\Theta)^\circ (c_p \pi^{n+1} + g\chi^{n+1}). \tag{D2}$$

To actually implement the scheme in full variables, and to avoid overly large excursions of the vertical velocity between the Euler forward and Euler backward step, we have rearranged the pressure solver to yield the Exner pressure update $\delta\pi^{n+1} = \pi^{n+1} - \pi^n$, so that the last expression becomes

$$c_p(P\Theta)^\circ \pi_z'^{n+1} + g\tilde{\chi}^{n+1}/\chi^\circ = (P\Theta)^\circ[c_p\delta\pi^{n+1} + (c_p\pi^n + g\chi^{n+1})]. \tag{D3}$$

The full variable version of the Euler forward and backward steps then follows straightforwardly from (24)–(28) by the appropriate replacements. The full variable scheme was implemented as an option in our scheme and produced results indistinguishable from the perturbation version for all the internal gravity wave tests.

Note that the explicit advection step should only account for the effect of potential temperature perturbations on the full potential temperature advection, since the advection of the background is covered by the linearized implicit step. There are various options for implementing this in a full variable formulation. One option, and the one we used in a first implementation, is to simply subtract the background before the advection step and add it back after it.

REFERENCES

Almgren, A. S., J. B. Bell, P. Colella, L. H. Howell, and M. L. Welcome, 1998: A conservative adaptive projection method for the variable density incompressible Navier–Stokes equations. *J. Comput. Phys.*, **142**, 1–46, https://doi.org/10.1006/jcph.1998.5890.

——, ——, C. A. Rendleman, and M. Zingale, 2006: Low Mach number modeling of type Ia supernovae. I. Hydrodynamics. *Astrophys. J.*, **637**, 922–936, https://doi.org/10.1086/498426.

Arakawa, A., and C. S. Konor, 2009: Unification of the anelastic and quasi-hydrostatic systems of equations. *Mon. Wea. Rev.*, **137**, 710–726, https://doi.org/10.1175/2008MWR2520.1.

Baldauf, M., and S. Brdar, 2013: An analytic solution for linear gravity waves in a channel as a test for numerical models using the non-hydrostatic, compressible Euler equations. *Quart. J. Roy. Meteor. Soc.*, **139**, 1977–1989, https://doi.org/10.1002/qj.2105.

Bannon, P. R., 1996: On the anelastic approximation for a compressible atmosphere. *J. Atmos. Sci.*, **53**, 3618–3628, https://doi.org/10.1175/1520-0469(1996)053<3618:OTAAFA>2.0.CO;2.

Bell, J. B., P. Colella, and H. Glaz, 1989: A second order projection method for the incompressible Navier Stokes equations. *J. Comput. Fluids*, **85**, 257–283, https://doi.org/10.1016/0021-9991(89)90151-4.

Benacchio, T., 2014: A blended semi-implicit numerical model for weakly compressible atmospheric dynamics. Ph.D. thesis, Freie Universität Berlin, XII+92 pp., http://edocs.fu-berlin.de/diss/receive/FUDISS_thesis_000000097149.

——, and N. Wood, 2016: Semi-implicit semi-Lagrangian modelling of the atmosphere: A Met Office perspective. *Commun. Appl. Ind. Math.*, **7**, 4–25, https://doi.org/10.1515/caim-2016-0020.

——, W. O'Neill, and R. Klein, 2014: A blended soundproof-to-compressible model for atmospheric dynamics. *Mon. Wea. Rev.*, **142**, 4416–4438, https://doi.org/10.1175/MWR-D-13-00384.1.

Bénard, P., J. Vivoda, J. Mašek, P. Smolíková, K. Yessad, C. Smith, R. Brožková, and J.-F. Geleyn, 2010: Dynamical kernel of the Aladin–NH spectral limited-area model: Revised formulation and sensitivity experiments. *Quart. J. Roy. Meteor. Soc.*, **136**, 155–169, https://doi.org/10.1002/qj.522.

Bryan, G. H., and J. M. Fritsch, 2002: A benchmark simulation for moist nonhydrostatic numerical models. *Mon. Wea. Rev.*, **130**, 2917–2928, https://doi.org/10.1175/1520-0493(2002)130<2917:ABSFMN>2.0.CO;2.

Bubnová, R., G. Hello, P. Bénard, and J.-F. Geleyn, 1995: Integration of the fully elastic equations cast in the hydrostatic pressure terrain-following coordinate in the framework of the ARPEGE/Aladin NWP system. *Mon. Wea. Rev.*, **123**, 515–535, https://doi.org/10.1175/1520-0493(1995)123<0515:IOTFEE>2.0.CO;2.

Cullen, M., 2007: Modelling atmospheric flows. *Acta Numer.*, **16**, 67–154, https://doi.org/10.1017/S0962492906290019.

——, and H. Maroofi, 2003: The fully compressible semi-geostrophic system from meteorology. *Arch. Ration. Mech. Anal.*, **167**, 309–336, https://doi.org/10.1007/s00205-003-0245-x.

Davies, T., A. Staniforth, N. Wood, and J. Thuburn, 2003: Validity of anelastic and other equation sets as inferred from normal-mode analysis. *Quart. J. Roy. Meteor. Soc.*, **129**, 2761–2775, https://doi.org/10.1256/qj.02.1951.

Dukowicz, J. K., 2013: Evaluation of various approximations in atmosphere and ocean modeling based on an exact treatment of gravity wave dispersion. *Mon. Wea. Rev.*, **141**, 4487–4506, https://doi.org/10.1175/MWR-D-13-00148.1.

Dumbser, M., D. Balsara, M. Tavelli, and F. Fambri, 2019: A divergence-free semi-implicit finite volume scheme for ideal, viscous, and resistive magnetohydrodynamics. *Int. J. Numer. Methods Fluids*, **89**, 16–42, https://doi.org/10.1002/fld.4681.

Durran, D. R., 1989: Improving the anelastic approximation. *J. Atmos. Sci.*, **46**, 1453–1461, https://doi.org/10.1175/1520-0469(1989)046<1453:ITAA>2.0.CO;2.

Giraldo, F. X., and M. Restelli, 2008: A study of spectral element and discontinuous Galerkin methods for the Navier–Stokes equations in nonhydrostatic mesoscale atmospheric modeling: Equation sets and test cases. *J. Comput. Phys.*, **227**, 3849–3877, https://doi.org/10.1016/j.jcp.2007.12.009.

Hairer, E., C. Lubich, and G. Wanner, 2006: *Geometric Numerical Integration: Structure-Preserving Algorithms for Ordinary Differential Equations*. Springer Series in Computational Mathematics, Vol. 31, 2nd ed. Springer, 644 pp., https://doi.org/10.1007/3-540-30666-8.

Hortal, M., 2002: The development and testing of a new two-time-level semi-Lagrangian scheme (SETTLS) in the ECMWF forecast model. *Quart. J. Roy. Meteor. Soc.*, **128**, 1671–1687, https://doi.org/10.1002/qj.200212858314.

Hoskins, B. J., and F. P. Bretherton, 1972: Atmospheric frontogenesis models: Mathematical formulation and solution. *J. Atmos. Sci.*, **29**, 11–37, https://doi.org/10.1175/1520-0469(1972)029<0011:AFMMFA>2.0.CO;2.

Jin, S., 2012: Asymptotic preserving (AP) schemes for multiscale kinetic and hyperbolic equations: A review. *Riv. Mat. Univ. Parma*, **3**, 177–216.

Kadioglu, S. Y., R. Klein, and M. L. Minion, 2008: A fourth-order auxiliary variable projection method for zero-Mach number gas dynamics. *J. Comput. Phys.*, **227**, 2012–2043, https://doi.org/10.1016/j.jcp.2007.10.008.

Klein, R., 2009: Asymptotics, structure, and integration of sound-proof atmospheric flow equations. *Theor. Comput. Fluid Dyn.*, **23**, 161–195, https://doi.org/10.1007/s00162-009-0104-y.

——, 2010: Scale-dependent asymptotic models for atmospheric flows. *Annu. Rev. Fluid Mech.*, **42**, 249–274, https://doi.org/10.1146/annurev-fluid-121108-145537.

——, and T. Benacchio, 2016: A doubly blended model for multiscale atmospheric dynamics. *J. Atmos. Sci.*, **73**, 1179–1186, https://doi.org/10.1175/JAS-D-15-0323.1.

——, N. Botta, L. Hofmann, A. Meister, C. Munz, S. Roller, and T. Sonar, 2001: Asymptotic adaptive methods for multiscale problems in fluid mechanics. *J. Eng. Math.*, **39**, 261–343, https://doi.org/10.1023/A:1004844002437.

——, U. Achatz, D. Bresch, O. M. Knio, and P. K. Smolarkiewicz, 2010: Regime of validity of sound-proof atmospheric flow models. *J. Atmos. Sci.*, **67**, 3226–3237, https://doi.org/10.1175/2010JAS3490.1.

Kühnlein, C., W. Deconinck, R. Klein, S. Malardel, Z. P. Piotrowski, P. K. Smolarkiewicz, J. Szmelter, and N. P. Wedi, 2019: FVM 1.0: A nonhydrostatic finite-volume dynamical core formulation for IFS. *Geosci. Model Dev.*, **12**, 651–676, https://doi.org/10.5194/gmd-12-651-2019.

Laprise, R., 1992: The Euler equations of motion with hydrostatic pressure as an independent variable. *Mon. Wea. Rev.*, **120**, 197–207, https://doi.org/10.1175/1520-0493(1992)120<0197:TEEOMW>2.0.CO;2.

Lipps, F., and R. Hemler, 1982: A scale analysis of deep moist convection and some related numerical calculations. *J. Atmos. Sci.*, **39**, 2192–2210, https://doi.org/10.1175/1520-0469(1982)039<2192:ASAODM>2.0.CO;2.

Marras, S., and Coauthors, 2016: A review of element-based Galerkin methods for numerical weather prediction: Finite elements, spectral elements, and discontinuous Galerkin. *Arch. Comput. Methods Eng.*, **23**, 673–722, https://doi.org/10.1007/s11831-015-9152-1.

Melvin, T., M. Dubal, N. Wood, A. Staniforth, and M. Zerroukat, 2010: An inherently mass-conserving iterative semi-implicit semi-Lagrangian discretization of the non-hydrostatic vertical-slice equations. *Quart. J. Roy. Meteor. Soc.*, **136**, 799–814, https://doi.org/10.1002/qj.603.

——, T. Benacchio, B. Shipway, N. Wood, J. Thuburn, and C. J. Cotter, 2019: A mixed finite-element, finite-volume, semi-implicit discretization for atmospheric dynamics: Cartesian geometry. *Quart. J. Roy. Meteor. Soc.*, https://doi.org/10.1002/qj.3501, in press.

Mengaldo, G., A. Wyszogrodzki, M. Diamantakis, S.-J. Lock, F. X. Giraldo, and N. P. Wedi, 2019: Current and emerging time-integration strategies in global numerical weather and climate prediction. *Arch. Comput. Methods Eng.*, **26**, 663–684, https://doi.org/10.1007/s11831-018-9261-8.

Pedlosky, J., Ed., 1992: *Geophysical Fluid Dynamics*. 2nd ed. Springer, 710 pp.

Prusa, J. M., P. K. Smolarkiewicz, and A. A. Wyszogrodzki, 2008: EULAG, a computational model for multiscale flows. *Comput. Fluids*, **37**, 1193–1207, https://doi.org/10.1016/j.compfluid.2007.12.001.

Restelli, M., and F. X. Giraldo, 2009: A conservative discontinuous Galerkin semi-implicit formulation for the Navier–Stokes equations in nonhydrostatic mesoscale modeling. *SIAM J. Sci. Comput.*, **31**, 2231–2257, https://doi.org/10.1137/070708470.

Schneider, T., N. Botta, K.-J. Geratz, and R. Klein, 1999: Extension of finite volume compressible flow solvers to multi-dimensional, variable density zero Mach number flow. *J. Comput. Phys.*, **155**, 248–286, https://doi.org/10.1006/jcph.1999.6327.

Skamarock, W. C., and J. B. Klemp, 1994: Efficiency and accuracy of the Klemp–Wilhelmson time-splitting technique. *Mon. Wea. Rev.*, **122**, 2623–2630, https://doi.org/10.1175/1520-0493(1994)122<2623:EAAOTK>2.0.CO;2.

Smolarkiewicz, P. K., and A. Dörnbrack, 2008: Conservative integrals of adiabatic Durran's equations. *Int. J. Numer. Methods Fluids*, **56**, 1513–1519, https://doi.org/10.1002/fld.1601.

——, and L. O. Margolin, 1993: On forward-in-time differencing for fluids: Extension to a curvilinear framework. *Mon. Wea. Rev.*, **121**, 1847–1859, https://doi.org/10.1175/1520-0493(1993)121<1847:OFITDF>2.0.CO;2.

——, and L. G. Margolin, 1997: On forward-in-time differencing for fluids: An Eulerian/semi-Lagrangian non-hydrostatic model for stratified flows. *Atmos.–Ocean*, **35**, 127–157, https://doi.org/10.1080/07055900.1997.9687345.

Smolarkiewicz, P., C. Kühnlein, and N. Wedi, 2014: A consistent framework for discrete integrations of soundproof and compressible PDEs of atmospheric dynamics. *J. Comput. Phys.*, **263**, 185–205, https://doi.org/10.1016/j.jcp.2014.01.031.

Smolarkiewicz, P. K., W. Deconinck, M. Hamrud, C. Kühnlein, G. Mozdzynski, J. Szmelter, and N. P. Wedi, 2016: A finite-volume module for simulating global all-scale atmospheric flows. *J. Comput. Phys.*, **314**, 287–304, https://doi.org/10.1016/j.jcp.2016.03.015.

——, C. Kühnlein, and N. P. Wedi, 2019: Semi-implicit integrations of perturbation equations for all-scale atmospheric dynamics. *J. Comput. Phys.*, **376**, 145–159, https://doi.org/10.1016/j.jcp.2018.09.032.

Straka, J. M., R. B. Wilhelmson, L. J. Wicker, J. R. Anderson, and K. K. Droegemeier, 1993: Numerical solutions of a non-linear density current: A benchmark solution and comparisons. *Int. J. Numer. Methods Fluids*, **17**, 1–22, https://doi.org/10.1002/fld.1650170103.

Strang, G., 1968: On the construction and comparison of difference schemes. *SIAM J. Numer. Anal.*, **5**, 506–517, https://doi.org/10.1137/0705041.

Sweby, P. K., 1984: High resolution schemes using flux limiters for hyperbolic conservation laws. *SIAM J. Numer. Anal.*, **21**, 995–1011, https://doi.org/10.1137/0721062.

Temperton, C., M. Hortal, and A. Simmons, 2001: A two-time-level semi-Lagrangian global spectral model. *Quart. J. Roy. Meteor. Soc.*, **127**, 111–127, https://doi.org/10.1002/qj.49712757107.

Van der Vorst, H. A., 1992: Bi-CGSTAB: A fast and smoothly converging variant of Bi-CG for the solution of nonsymmetric linear systems. *SIAM J. Sci. Stat. Comput.*, **13**, 631–644, https://doi.org/10.1137/0913035.

Van Leer, B., 2006: Upwind and high-resolution methods for compressible flow: From donor cell to residual-distribution schemes. *16th AIAA Computational Fluid Dynamics Conf.*, Orlando, FL, American Institute of Aeronautics and Astronautics, AIAA 2003-3559, https://doi.org/10.2514/6.2003-3559.

Vater, S., and R. Klein, 2009: Stability of a projection method for the zero Froude number shallow water equations. *Numer. Math.*, **113**, 123–161, https://doi.org/10.1007/s00211-009-0224-8.

Weller, H., and A. Shahrokhi, 2014: Curl-free pressure gradients over orography in a solution of the fully compressible Euler equations with implicit treatment of acoustic and gravity waves. *Mon. Wea. Rev.*, **142**, 4439–4457, https://doi.org/10.1175/MWR-D-14-00054.1.

Wood, N., and Coauthors, 2014: An inherently mass-conserving semi-implicit semi-Lagrangian discretization of the deep-atmosphere global non-hydrostatic equations. *Quart. J. Roy. Meteor. Soc.*, **140**, 1505–1520, https://doi.org/10.1002/qj.2235.